Phosphorylation-dependent membraneless organelle fusion and fission illustrated by postsynaptic density assemblies
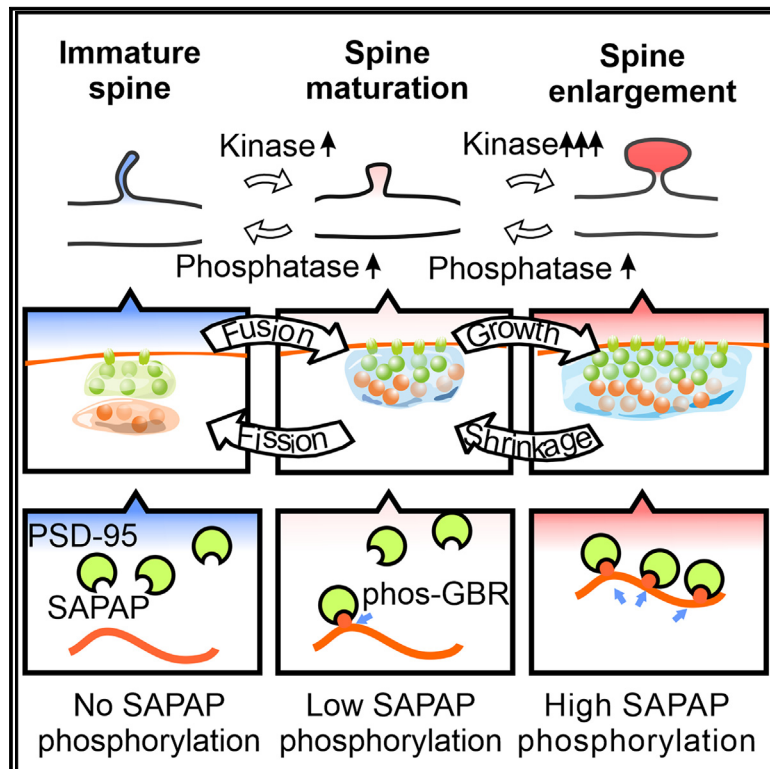
Graphical abstract

Highlights

- A reconstituted PSD protein mixture forms two distinct condensates via phase separation

- Phosphorylation of SAPAP, a linker protein, leads to fusion of the two condensates

- Dephosphorylation of the linker protein causes fission of the fused condensates

- Membraneless organelles can undergo regulated fusion and fission

Authors

Haowei Wu, Xudong Chen, Zeyu Shen, Hao Li, Shiqi Liang, Youming Lu, Mingjie Zhang

Correspondence

zhangmj@sustech.edu.cn

In brief

Using a partially reconstituted postsynaptic density protein assembly, Wu et al. demonstrate that membraneless organelles formed via phase separation can also undergo regulated fusion and fission analogous to membrane-based organelles.

CellPress

Article

Phosphorylation-dependent membraneless organelle fusion and fission illustrated by postsynaptic density assemblies

Haowei Wu,[1,6] Xudong Chen,[1,6] Zeyu Shen,[1] Hao Li,[2,3] Shiqi Liang,[2,3] Youming Lu,[2,3] and Mingjie Zhang[4,5,7,*]

[1]Division of Life Science, State Key Laboratory of Molecular Neuroscience, Hong Kong University of Science and Technology, Clear Water Bay, Kowloon, Hong Kong, China
[2]Department of Pathophysiology, School of Basic Medicine and Tongji Medical College, Huazhong University of Science and Technology, Wuhan 430030, China
[3]The Institute for Brain Research, Collaborative Innovation Center for Brain Science, Huazhong University of Science and Technology, Wuhan 430030, China
[4]Greater Bay Biomedical Innocenter, Shenzhen Bay Laboratory, Shenzhen 518036, China
[5]School of Life Sciences, Southern University of Science and Technology, Shenzhen 518055, China
[6]These authors contributed equally
[7]Lead contact
*Correspondence: zhangmj@sustech.edu.cn
https://doi.org/10.1016/j.molcel.2023.11.011

SUMMARY

Membraneless organelles formed by phase separation of proteins and nucleic acids play diverse cellular functions. Whether and, if yes, how membraneless organelles in ways analogous to membrane-based organelles also undergo regulated fusion and fission is unknown. Here, using a partially reconstituted mammalian postsynaptic density (PSD) condensate as a paradigm, we show that membraneless organelles can undergo phosphorylation-dependent fusion and fission. Without phosphorylation of the SAPAP guanylate kinase domain-binding repeats, the upper and lower layers of PSD protein mixtures form two immiscible sub-compartments in a phase-in-phase organization. Phosphorylation of SAPAP leads to fusion of the two sub-compartments into one condensate accompanied with an increased Stargazin density in the condensate. Dephosphorylation of SAPAP can reverse this event. Preventing SAPAP phosphorylation in vivo leads to increased separation of proteins from the lower and upper layers of PSD sub-compartments. Thus, analogous to membrane-based organelles, membraneless organelles can also undergo regulated fusion and fission.

INTRODUCTION

Eukaryotic cells are highly compartmentalized. Historically, it is generally understood that cellular compartmentalization is achieved by forming various sub-cellular organelles demarcated by lipid membranes. These membrane-enclosed organelles are dynamic and can undergo extensive remodeling, including organelle fusion or fission, in response to specific cellular signals. Recent work has revealed another category of cellular organelles that are formed via phase separation or phase transition of proteins and nucleic acids.[1–7] These recently recognized cellular organelles formed via phase separation are either devoid of or not enclosed by lipid membranes, and thus such organelles are frequently referred to as membraneless organelles. Membraneless organelles are now known to function in broad spectrums of cellular processes including gene transcription and translation, cell growth and proliferation, inter- and intra-cellular signaling, etc.[6,8–10] Membraneless organelles can also interact with membrane-based organelles to orchestrate numerous

cellular processes such as cell polarization, cellular autophagy, neuronal- or immune-synapse formation, etc.[5,11–13] It is well accepted that membraneless organelles, upon contact, can undergo spontaneous homotypic fusion to minimize surface tensions of the organelle droplets.[4,14] It is also well accepted that formation and dispersion of membraneless organelles are regulated processes.[15,16] However, little is known about whether membraneless organelles, in a way analogous to membrane-based organelles, may also undergo fusion or fission in response to specific cellular signals.

The postsynaptic density (PSD) of excitatory neuronal synapses is an example of a membraneless organelle formed by scaffold proteins and their interacting neurotransmitter receptors and synaptic signaling enzymes.[17–19] In response to stimulations, PSDs of neuronal synapses can undergo bidirectional changes in their sizes (PSDs are disc-shaped molecular assemblies underneath postsynaptic membranes, and their sizes are generally measured by the areas of PSDs).[20–22] The size of the PSD is linearly correlated with the electric strength of a synapse, as the
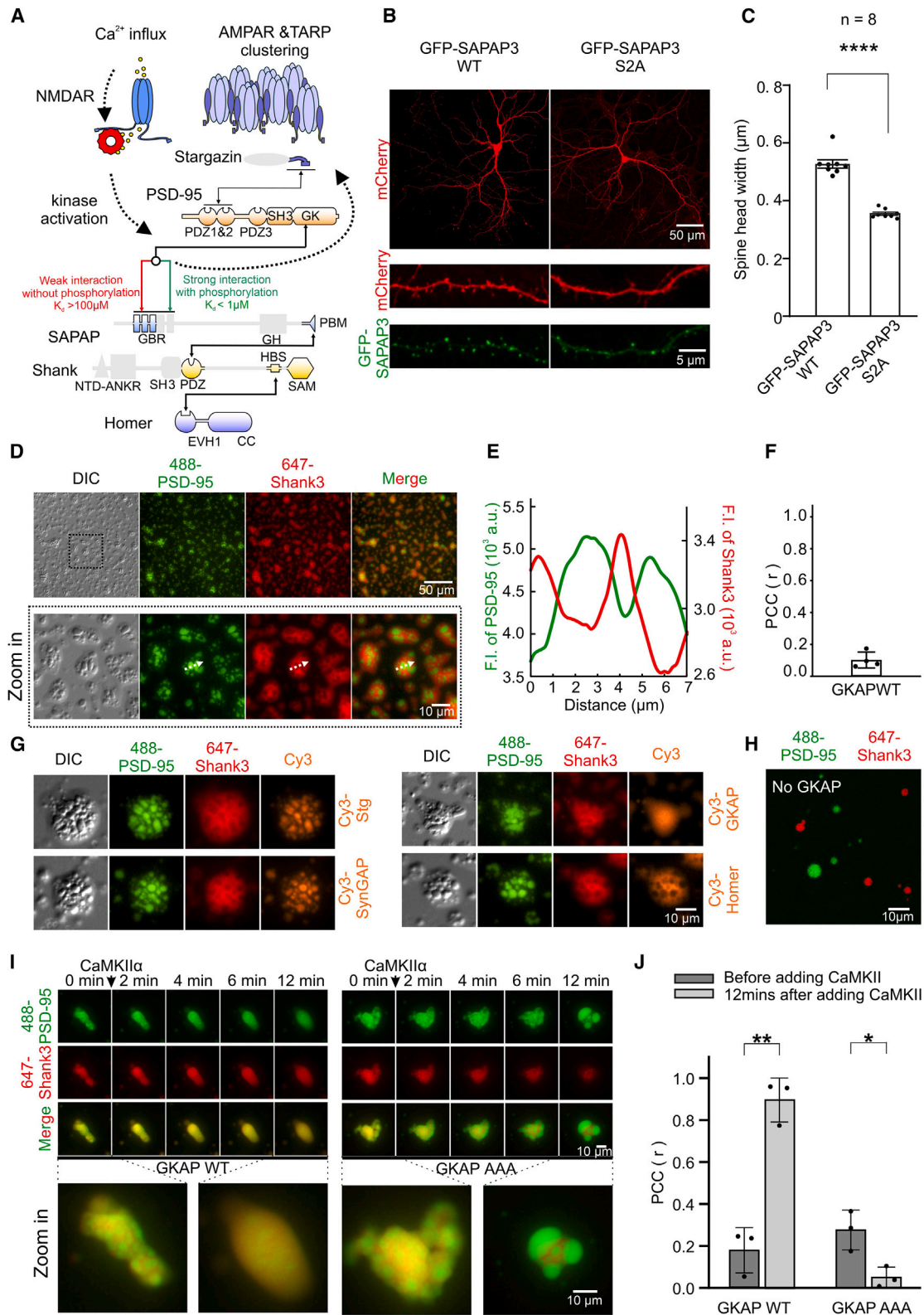
(legend on next page)

total number and density of neurotransmitter receptors in the PSD are proportional to the size of the PSD.[23–26] Electron microscopic studies of PSDs revealed that PSDs are sub-compartmentalized, containing a denser layer of PSD core with a thickness of ~30 nm right beneath the synaptic plasma membrane (referred to as the PSD core or the upper layer of the PSD) followed by a less dense layer of protein assembly with a thickness of ~50 nm (also known as the PSD pallium or the lower layer of PSD).[27] Glutamate receptors and the PSD-95 scaffold are enriched in the PSD core sub-compartment, and scaffold proteins including Shank and Homer are enriched in the PSD pallium.[27–32] The SAPAP family scaffold proteins serve as molecular linkers in connecting the two layers of PSDs forming the PSD assemblies[3,18,33] (Figure 1A). Fittingly, SAPAPs have been observed to be present in both the upper and lower layers of PSDs by electron microscopy (EM).[27,33,34] When a synapse is stimulated, the entire PSD becomes thicker and denser,[22,26,35–38] a process involving addition of proteins to the PSD assembly, which can enhance phase separation[18] and other cellular processes such as new protein synthesis, altered molecular interaction among PSD proteins, cytoskeletal structure alterations, etc.[39–45] The boundary between the PSD core and pallium also becomes less obvious,[36] indicating that the two layers of PSD are more uniform in their molecular densities. Importantly, such activity-dependent PSD thickening is accompanied with an acute accumulation of calmodulin-dependent kinase II (CaMKII) in PSD.[35,43,46,47] Inhibiting the kinase activity of CaMKII also blocks the activity-induced synapse and PSD growth,[48,49] whereas blocking the activity of phosphatases prolongs the activity-induced PSD thickening.[50]

Among numerous CaMKII substrates in the PSD, the SAPAP family scaffold proteins are particularly interesting. Each SAPAP protein contains 2–5 short, PSD-95-binding repeat sequences at the N-terminal end. Each of these repeats is with ~15 amino acid residues and can bind to the guanylate kinase (GK) domain of PSD-95 (hence the repeats are also known as GK-binding repeats or "GBRs" in short).[51,52] A striking feature is that the interactions between the native GBRs and PSD-95 GK are extremely weak (K_D >100 μM).[18,51] Upon phosphorylation of a completely conserved Ser in any one or more of the repeat sequences, the interaction between phospho-SAPAP and PSD-95 is enhanced by ~1,000-fold, leading to the formation of very stable SAPAP/PSD-95 complexes[51,53,54] (Figure 1A). The same Ser residues in SAPAP GBRs can also be phosphorylated by protein kinase C (PKC) in vitro.[51] Thus, we hypothesized that phosphorylation of SAPAP may serve as a molecular switch in connecting the upper core and the lower pallial layers of PSD sub-compartments, together forming an intact, thickened PSD upon synaptic stimulation.

Here, we partially reconstitute the upper layer of the PSD with the Stargazin (Stg) tail and PSD-95 and the lower layer of the PSD with truncated Shank3, a simplified form of SAPAP and Homer1. The reconstituted PSD protein mixture formed two distinct sub-compartments via phase separation. The two sub-compartments are arranged in a phase-in-phase pattern with SAPAP evenly distributed in both sub-compartments. Phosphorylation of SAPAP leads to fusion of the two distinct sub-compartments into a uniform condensate. Dephosphorylation of SAPAP induces fission of the single PSD assembly into two sub-compartments. We designed a genetically encodable and stable PSD-95-binding SAPAP mutant that can effectively mimic constitutively phosphorylated SAPAP. We demonstrate that the enhanced SAPAP/PSD-95 interaction induced by SAPAP phosphorylation supports synaptic growth in cultured neurons. Strikingly, preventing the two sub-compartments of PSD from interacting with each other in vivo by blocking SAPAP phosphorylation leads to separation of scaffold proteins from the two layers of the PSD sub-compartments.
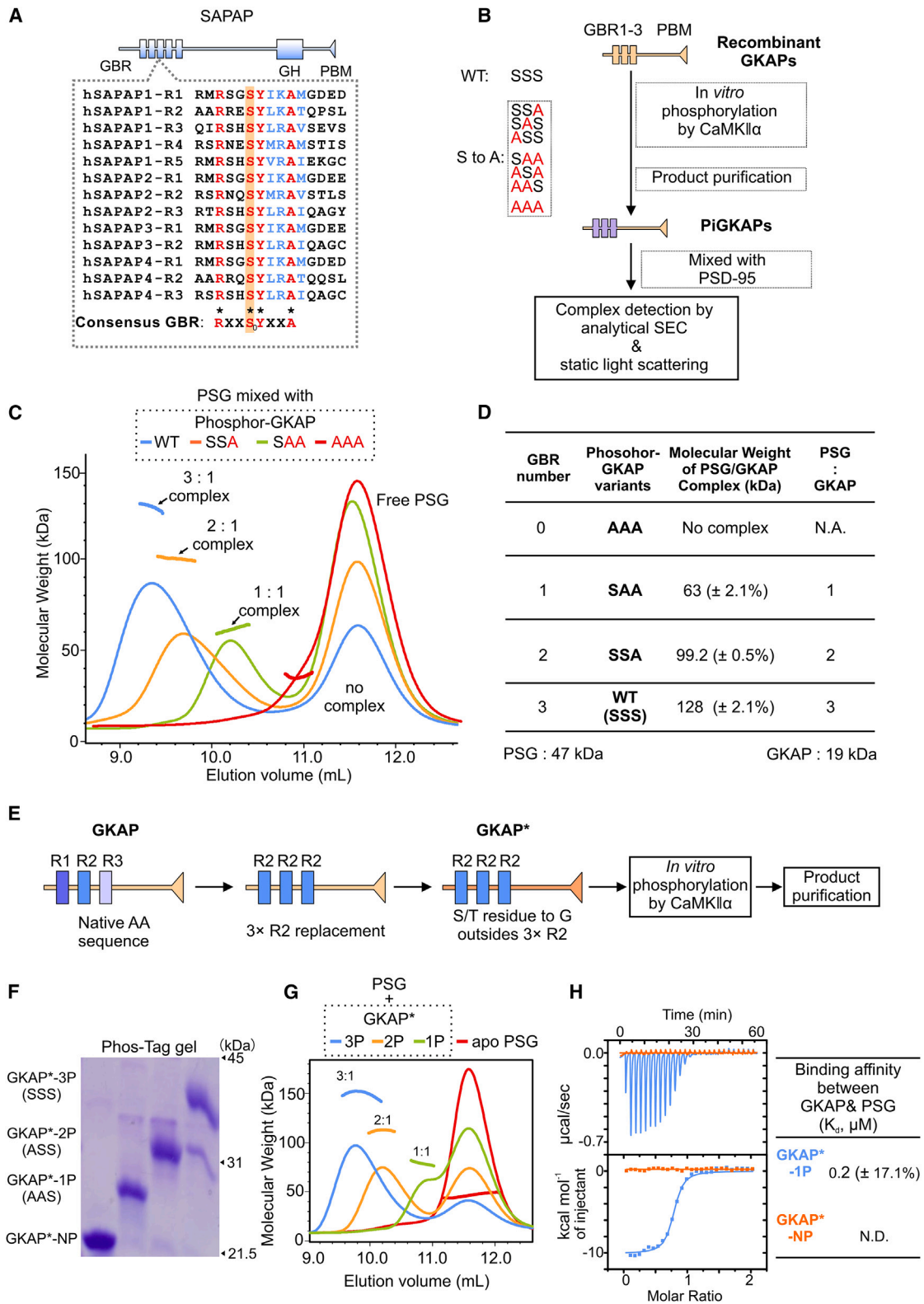
RESULTS

Phosphorylation of SAPAP modulates synaptic growth

To test potential roles of SAPAP phosphorylation on synaptic growth, we transfected GFP-SAPAP3 wild type (WT) or a GFP-SAPAP3 S2A mutant, in which the CaMKII-targeting Ser

Figure 1. CaMKIIα triggers the fusion of two immiscible PSD sub-compartments

(A) Schematic diagram showing the molecular components of the PSD protein network. The interaction details among PSD proteins are indicated by two arrowheaded lines. Domains drawn in gray are removed from the corresponding proteins.

(B) Representative images of cultured mice hippocampal neurons transfected with GFP-SAPAP3 WT or GFP-SAPAP3 S2A.

(C) Quantification of image data in (B) showing increased spine head width in neurons expressing SAPAP3 WT, when compared with neurons expressing GFP-SAPAP3 S2A. Error bars indicate ± SD. ****p < 0.0001. Student's t test.

(D) DIC/fluorescence microscopy images showing two immiscible PSD sub-compartments enriched with iFluor-488-labeled (at 2% sparse labeling) PSD-95 or Alexa 647-labeled (also 2% labeling) Shank3, respectively. The protein labeling ratio was used throughout the study, unless otherwise stated. Stg, PSD-95, GKAP, SynGAP, Shank3, and Homer1 were all at 10 μM.

(E) Fluorescence intensity line scanning plots showing the segregated distribution of iFluor-488-labeled PSD-95 and Alexa 647-labled Shank3 into two distinct sub-compartments in (D).

(F) Quantification of co-localization of two sub-compartments in (D). Pearson's correlation coefficient (PCC) is with a range from 0 to 1, with the value 0 standing for two phases totally immiscible and value 1 meaning the two phases are completely mixed. Error bar indicates ± SD.

(G) DIC/fluorescence microscopy images showing the localization of Cy3-labeled Stg, SynGAP, GKAP, and Homer1, respectively, in the two segregated condensates. Stg, PSD-95, GKAP, SynGAP, Shank3, and Homer1 were all at 10 μM.

(H) Confocal microscopy images showing that dropout of GKAP from the reconstitution system in (G) led to complete separation of the Stg/PSD-95/SynGAP condensate from the Shank3/Homer condensate. Stg, PSD-95, SynGAP, Shank3, and Homer1 were all at 10 μM.

(I) Time-lapse images showing that adding 1 μM CaMKIIα into segregated condensates formed by PSD-95, GKAP WT, Shank3, and Homer1 led to the fusion of PSD-95 sub-compartment with the Shank3 sub-compartment (left). In contrast, segregated condensates formed by GKAP AAA/Shank3/Homer1 failed to fuse with the PSD-95/Stg condensate, even in the presence of active CaMKIIα (right).

(J) Statistic Pearson's correlation coefficient (PCC) measuring the de-mixing of PSD-95 from Shank3 before and 12 min after CaMKIIα activation in (I). Error bars indicate ± SD. *p < 0.05 and **p < 0.01, using Student's t test.

A

SAPAP

GBR   GH   PBM

hSAPAP1-R1	RMRSGSYIKAMGDED
hSAPAP1-R2	AARRESYLKATQPSL
hSAPAP1-R3	QIRSHSYLRAVSEVS
hSAPAP1-R4	RSRNESYMRAMSTIS
hSAPAP1-R5	RMRSHSYVRAIEKGC
hSAPAP2-R1	RMRSGSYIKAMGDEE
hSAPAP2-R2	RSRNQSYMRAVSTLS
hSAPAP2-R3	RTRSHSYLRAIQAGY
hSAPAP3-R1	RMRSGSYIKAMGDEE
hSAPAP3-R2	RMRSHSYLRAIQAGC
hSAPAP4-R1	RMRSGSYIKAMGDED
hSAPAP4-R2	AARRQSYLRATQQSL
hSAPAP4-R3	RSRSHSYLRAIQAGC

Consensus GBR: RXXSYXXA

B

GBR1-3   PBM

WT: SSS

S to A: SSA
           SAS
           ASS
           SAA
           ASA
           AAS
           AAA

Recombinant GKAPs

In vitro phosphorylation by CaMKIIα

Product purification

PiGKAPs

Mixed with PSD-95

Complex detection by analytical SEC & static light scattering

C

PSG mixed with
Phosphor-GKAP
— WT — SSA — SAA — AAA

3 : 1 complex
2 : 1 complex
1 : 1 complex
Free PSG
no complex

Molecular Weight (kDa) vs Elution volume (mL)

D

GBR number	Phosohor-GKAP variants	Molecular Weight of PSG/GKAP Complex (kDa)	PSG : GKAP
0	**AAA**	No complex	N.A.
1	**SAA**	63 (± 2.1%)	1
2	**SSA**	99.2 (± 0.5%)	2
3	**WT (SSS)**	128 (± 2.1%)	3

PSG : 47 kDa   GKAP : 19 kDa

E

GKAP
R1 R2 R3
Native AA sequence

→ R2 R2 R2
3× R2 replacement

→ **GKAP***
R2 R2 R2
S/T residue to G outside 3× R2

→ In vitro phosphorylation by CaMKIIα

→ Product purification

F

Phos-Tag gel   (kDa)
◄45
GKAP*-3P (SSS)
GKAP*-2P (ASS)
◄31
GKAP*-1P (AAS)
GKAP*-NP
◄21.5

G

PSG + GKAP*
— 3P — 2P — 1P — apo PSG

3:1
2:1
1:1

Molecular Weight (kDa) vs Elution volume (mL)

H

Time (min)
μcal/sec

kcal mol⁻¹ of injectant

Molar Ratio

Binding affinity between GKAP & PSG (K_d, μM)	
GKAP*-1P	0.2 (± 17.1%)
GKAP*-NP	N.D.

(legend on next page)

residues in each of its two GBR sequences were replaced with Ala (see Figure 2A for the GBR sequences), to the cultured hippocampal neurons and measured the spine developments of transfected cells. Consistent with our previous findings,[51] neurons expressing SAPAP3 S2A displayed a significantly impaired synaptic maturation when compared with neurons expressing SAPAP3 WT (Figures 1B and 1C). Since the size of a dendritic spine is proportional to the electric strength of a synapse,[24–26] we reasoned that phosphorylation and dephosphorylation of SAPAPs might bidirectionally modulate synaptic transmission.

Reconstituted PSD contains two distinct sub-compartments linked by unphosphorylated SAPAPs

The sizes of dendritic spines posed technical challenges to investigating the mechanistic roles of SAPAP phosphorylation on PSD enlargement and consequent synapse maturation in living neurons. We resorted to the biochemically reconstituted PSDs that can serve as a unique platform for dissecting the molecular mechanisms underlying PSD formation and regulation.[18,19] We reconstituted a defined PSD assembly by mixing four most abundant PSD scaffold proteins (PSD-95, SAPAP1 also known as GKAP, Shank3, and Homer1), a synaptic-enriched enzyme SynGAP, and the cytoplasmic tail of Stg serving as a proxy of AMPA receptors (Figure 1A). We used a simplified version of recombinant SAPAP1 for our reconstitution studies. This version of SAPAP1 contained the first three GBRs fused to the C-terminal PDZ domain binding motif (PBM) (Figure 2B; we named this simplified protein GKAP to differentiate it from the native form of SAPAP1 in our following cellular and *in vivo* studies). Shank3 and SynGAP used in this study were also truncated with detailed boundary information specified in the key resources table. These recombinant proteins have been extensively characterized in our earlier studies.[18,19] Interestingly, mixing of these six PSD proteins (each at 10 μM) resulted in coexistence of two types of immiscible liquid droplets organized in a phase-in-phase pattern with clear boundaries under differential interference contrast (DIC) microscopy (Figure 1D). Fluorescence microscopic imaging revealed that PSD-95 (iFluor-488-labeled) was enriched in the inner condensates, and Shank3 (Alexa 647-labeled) was concentrated at the outer condensates, indicating that the reconstituted PSD assembly formed two distinct sub-compartments (Figures 1D and 1E; quantified in Figure 1F).

By assigning the third fluorophore (Cy3) individually to Stg, SynGAP, GKAP, or Homer1, we mapped the localizations of all other proteins inside the immiscible condensates using fluorescence microscopy. This imaging assay revealed that PSD-95-positive phase selectively enriched Stg and SynGAP, which are direct binders of PSD-95, whereas Shank3-positive phase specifically recruited Shank3-binding partner Homer1 (Figures 1G and S1). Interestingly, unphosphorylated GKAP was uniformly distributed in both phases (Figure 1G, the far-right panel). It is noted that the proteins in the PSD-95-positive phase are in the core layer of the PSD, and the proteins in the Shank3-positive phase match the pallial layer of the PSD. GKAP functions to connect and keep the two distinct phases together in a phase-in-phase pattern. Consistent with the tethering role of GKAP in keeping the two PSD sub-compartments in a phase-in-phase pattern, dropout of GKAP from the six-protein reconstituted PSD system led to complete separation of the Stg/PSD-95/SynGAP condensate from the Shank3/Homer1 condensate (Figure 1H).

CaMKIIα phosphorylation of GKAP triggers fusion of the two PSD sub-compartments

We then asked whether CaMKIIα might be able to modulate the PSD assembly organization via phosphorylation of GKAP. We mixed active CaMKIIα kinase domain (1 μM) with the six PSD proteins (each at 10 μM). Time-lapse imaging showed that the PSD-95-positive and Shank3-positive sub-compartments were initially immiscible in the absence of CaMKIIα, but they rapidly coalesced and became homogeneous after the addition of CaMKIIα. The fusion between the PSD-95-positive and Shank3-positive droplets could be observed at 2 min, and the fusion was essentially completed, and the condensates became uniform at 12 min after the CaMKIIα injection for a very large droplet (Figure 1I, left panel; quantified in Figure 1J).

The recombinant GKAP protein contained three different GBRs that are thought to be the substrates of CaMKIIα. We mutated the conserved Ser that is known as the CaMKII phosphorylation site in each GKAP GBR with Ala. The resulting CaMKIIα phosphorylation-null mutant was termed GKAP AAA. The six-PSD-protein mixture with GKAP AAA replacing GKAP WT still formed two immiscible condensates. However, such segregated

Figure 2. CaMKIIα regulates the interaction between SAPAP and PSD-95

(A) Schematic diagram showing the domain organizations of SAPAP family proteins (SAPAP1–4). The amino acid sequence alignment of GBR repeats of human SAPAPs is also shown. The absolutely conserved and conserved residues are colored in red and blue, respectively. The consensus GBR motif -R-X-X-S_0-Y-X-X-A- is shown beneath the alignment. S_0 is the CaMKIIα phosphorylation site.

(B) Schematic diagram showing the experimental steps for making different phosphor-GKAPs by *in vitro* CaMKIIα phosphorylation.

(C) Fast protein liquid chromatography (FPLC) coupled with static light scattering analysis measuring the complex formation of different phosphor-GKAPs with PSD-95 PSG. The fitted molecular mass of each complex peak matching the corresponding stoichiometric PSD-95 PSG/phosphor-GKAP complex is indicated above the peak.

(D) Table summarizing the measured molecular mass of each GKAP/PSG mixture in (C). The theoretical molecular masses of PSG and GKAP are 47 and 19 kDa, respectively.

(E) Schematic diagram showing the preparation of GKAP* for clean and optimized *in vitro* CaMKIIα phosphorylation.

(F) Phos-Tag SDS-PAGE assay showing the stoichiometric phosphorylation of GKAP* by CaMKIIα *in vitro*.

(G) FPLC coupled with static light scattering analysis measuring the complex formation between each of the three phosphor-GKAP*s and PSD-95 PSG. The stoichiometry of each PSD-95 PSG/phosphor-GKAP* complex formed is indicated above the peak.

(H) ITC measurements showing a high binding affinity between GKAP*-1P with PSD-95 PSG (blue curve). No interaction was detected between GKAP*-NP and PSD-95 PSG (orange curve). 200 μM GKAP* was titrated to 20 μM PSG.

condensates could no longer fuse upon addition of active CaM-KIIα (Figure 1I, right panel; quantified in Figure 1J). Thus, these imaging data indicate that CaMKII-mediated phosphorylation of the GBR sequences of GKAP is essential for the fusion of two PSD sub-compartments into a homogeneous condensate in this reconstitution system.

Characterization of phosphorylation-dependent interaction between PSD-95 and GKAP

The SAPAP family members contain highly conserved GBRs with different repeat numbers (Figure 2A). CaMKIIα phosphorylates the conserved Ser at the center of the GBRs, leading to a dramatically enhanced binding to the GK domain of PSD-95[51,53–55] (Figure 2A).

There are three GBRs in GKAP, and we asked whether all three GBRs on GKAP could be simultaneously phosphorylated by CaMKIIα to generate a multi-valent PSD-95-binding phosphor-GKAP. To achieve this goal, we generated eight GKAP mutants carrying all possible combinations of Ser-to-Ala substitutions on its GBRs (Figure 2B): GKAP WT containing three potential phosphorylation sites (GKAP SSS); the three single substitutions (GKAP SSA, SAS, and ASS), the three double substitutions (GKAP AAS, ASA, and SAA), and a triple substitution (GKAP AAA) (see Figure 2B for the schemes). Next, each of these eight purified GKAP variants was incubated with active CaMKIIα (at a 20:0.5 μM molar ratio) to allow for complete phosphorylation. CaMKII was then removed from each reaction mixture by a step of size exclusion chromatography (SEC). Each phosphorylated GKAP variant was mixed with the PDZ3-SH3-GK tandem of PSD-95 (PSG) at the final concentration of 40 μM GKAP and 160 μM PSD-95 PSG. The resulting complex formed between PSD-95 PSG and each GKAP variant was assayed by analytical SEC coupled with static light scattering analysis (Figure 2C).

This in vitro phosphorylation and complex formation assay clearly revealed a phosphorylation-dependent interaction between PSD-95 and GKAP. Phosphorylated GKAP WT formed the largest complex with PSD-95, with a fitted molecular weight of ∼130 kDa that approximately equals 1 GKAP bound to 3 copies of PSG (Figures 2C, blue curve and 2D). Phospho-GKAP variants carrying single Ser-to-Ala substitution on GBRs (SSA, SAS, and ASS) each also formed complexes with PSG, but the resulting complexes are with a molecular mass matching 1 GKAP bound to 2 PSG (Figures 2C, orange curve and 2D) (also see Figure S2). Phospho-GKAP variants with double Ser-to-Ala substitutions (SAA, ASA, and AAS) formed stable complexes with PSG, each with a molecular mass corresponding to a 1:1 GKAP/PSG complex (Figures 2C, green curve, 2D, and S2). As expected, no complex formation was detected when PSG was mixed with the GKAP variant with all three Ser replaced with Ala (Figures 2C, red curve and 2D). Thus, we concluded that all three GBRs on GKAP can be phosphorylated by CaMKIIα. Our biochemical data also hint that the GBR repeats of SAPAPs may serve as a detector for sensing the level and duration of CaMKII or PKC activation in synapses.

Design of phospho-GKAP for phase separation studies of PSD assembly

GKAP is a largely disordered protein. During our in vitro CaM-KIIα-mediated phosphorylation experiments, we detected

different levels of spurious phosphorylation of Ser or Thr residues outside the conserved Ser in GBRs (data not shown). This non-specific phosphorylation did not interfere with the interaction between GKAP and PSD-95 (Figures 2C and 2D). However, such non-specific phosphorylation was difficult to control and caused instabilities in subsequent in vitro phase separation experiments, as phase separation is sensitive to the charge properties of involved proteins. To perform clean and repeatable phase separation assays, we designed an improved version of GKAP (named GKAP*) in which no amino acids other than the Ser residue in the GBR sequences could be phosphorylated by CaM-KIIα by the following two steps (Figure 2E). First, the first and the third GBRs were changed to GBR2 as GBR2 only contains one Ser residue within the consensus GBR sequence (Figure 2A). We then substituted all remaining Ser/Thr residues outside GBRs on GKAP (except for the Thr residue at the C-terminal PBM motif for the specific GKAP/Shank interaction[56]) with Gly. The resulting GKAP* WT (SSS), GKAP* ASS (with Ser-to-Ala mutation on first GBR2), and GKAP* AAS (with Ser-to-Ala mutation on first and second GBR2) contain three, two, and one CaMKII phosphorylation sites, respectively. These GKAP* variants were individually and fully phosphorylated by CaMKIIα. The purity and the level of phosphorylation of the three phospho-GKAP* variants were confirmed by Phos-Tag coupled with SDS-PAGE analysis (Figure 2F). Analytical SEC assay showed that GKAP*-3P, -2P, and -1P could bind to 3, 2, and 1 copies of PSD-95 PSG, respectively (Figure 2G). Isothermal titration calorimetry (ITC) experiments showed a strong binding of PSD-95 PSG to GKAP*-1P but no binding to unphosphorylated GKAP* (GKAP*-NP) (Figure 2H). Together, the above biochemical data reveal that the GKAP* variants designed can achieve clean and complete phosphorylation by CaMKII, and these GKAP variants exhibit the same phosphorylation-dependent interactions with PSD-95 as GKAP WT does.

Phosphorylation of single GBR of GKAP causes formation of single-phase PSD assembly that can fission into two sub-compartments by PP2A

We then asked whether single phosphorylated GKAP*-1P, which has an enhanced binding affinity to PSD-95, is sufficient to cause PSD-95-positive and Shank3-positive condensates to coalesce together. As shown by imaging data, the designed GKAP*-NP behaved like GKAP WT in forming two distinct PSD-95-positive and Shank3-positive sub-compartments (Figures 3A and 3B; quantified in Figure 3E). However, replacing GKAP*-NP with GKAP*-1P completely abolished immiscibility of the two PSD sub-compartments (Figures 3C and 3D; quantified in Figure 3E), indicating that phosphorylation of single GBR of GKAP is sufficient to cause two PSD sub-compartments to fuse into one homogeneous compartment. This result hints that even when only a fraction of SAPAPs is phosphorylated, the phosphorylated SAPAPs can assemble stable PSD assembly containing perhaps a portion of key scaffold proteins including PSD-95, Shank, and Homer.

We used single-molecule tracking to measure the dynamics of PSD-95 and Shank3 in the PSD mixtures before and after GKAP phosphorylation, following the procedure described in our recent study.[57] For each single-molecule tracking
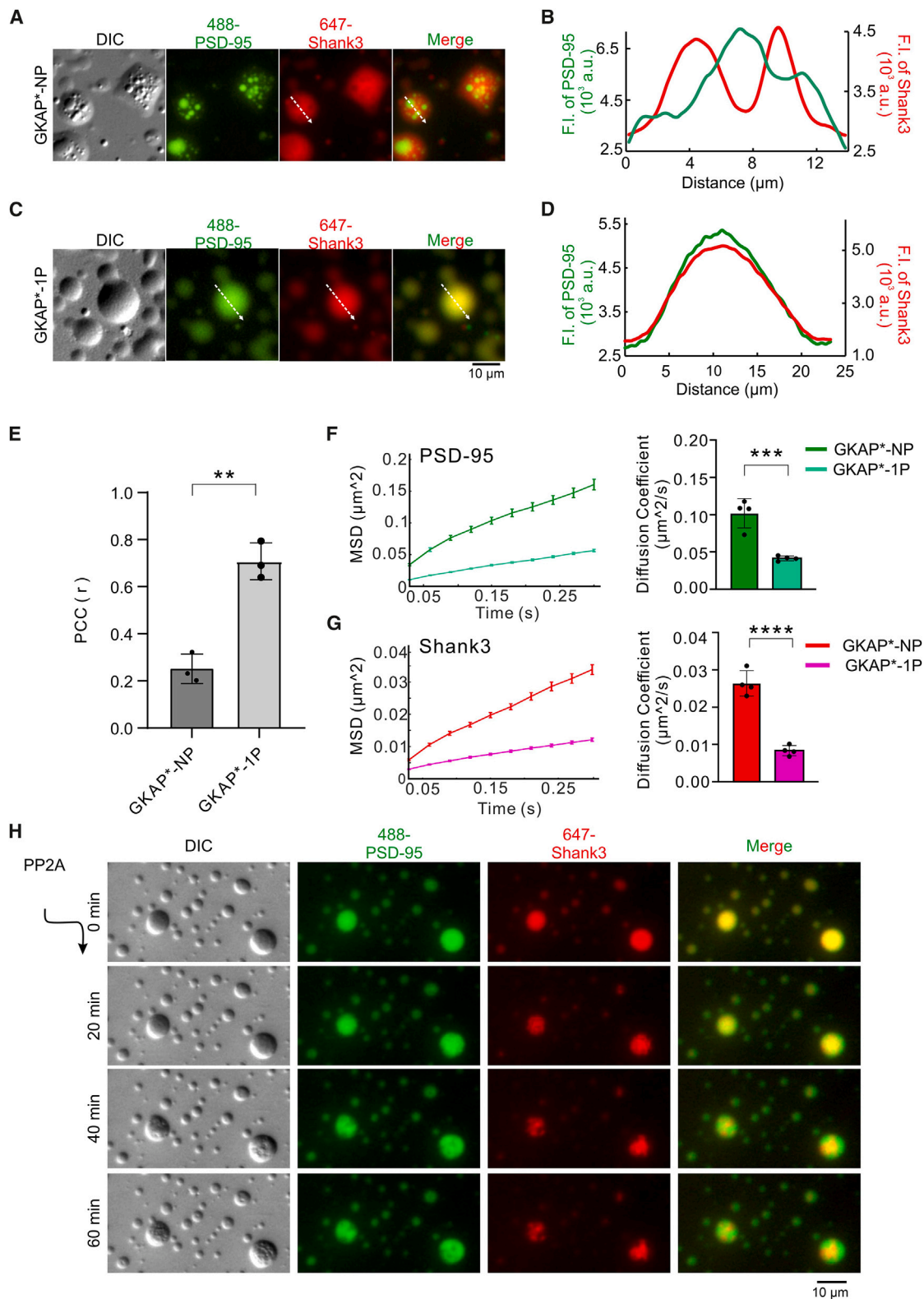
Figure 3. Phosphorylation on the GBR of GKAP is sufficient to achieve the fusion of two immiscible PSD sub-compartments

(A) DIC/fluorescence microscopy images showing two immiscible PSD sub-compartments were formed by 10 μM Stg, PSD-95, GKAP*-NP, Shank3, and Homer1.

experiment, only one protein was very sparsely labeled with Cy3 (at 0.01%). We used GKAP*-NP or GKAP*-1P to mix with Stg, PSD-95, Shank3, and Homer1 to represent the system before and after CaMKIIα-mediated phosphorylation of GKAP. As shown in Figures 3F and 3G, the diffusion coefficient of PSD-95 and Shank3 became significantly lower after GKAP was phosphorylated. The GKAP phosphorylation-induced mobility decreases of PSD-95 and Shank3 can be explained by increased network complexity and stability of the PSD protein assembly due to the enhanced interaction between PSD-95 and phosphorylated GKAP.[57]

PSD is an efficient signal-transduction machinery containing a vast pool of protein kinases and phosphatases, and the coordination of protein phosphorylation/dephosphorylation provides molecular bases for bidirectional modulations of PSD formation and synaptic strengths.[58–60] We wondered whether GKAP phosphorylation-induced condensate fusion could be reversed by PP2A, a protein phosphatase known to be enriched in the PSD.[61] We added 1 μM purified PP2A to the single-phase PSD assembly formed by the five PSD proteins, among which GKAP was replaced with GKAP*-1P. DIC imaging showed that the PSD assembly was initially homogeneous but became progressively heterogeneous in the presence of PP2A (Figure 3H, left panel). Fluorescence microcopy imaging revealed that PSD-95 and Shank3 became gradually segregated into two immiscible sub-compartments (Figure 3H, right three panels). These imaging data revealed that dephosphorylation of GKAP can cause fission of the single-phase PSD assembly into two distinct sub-compartments.

Phosphorylation of multiple GBRs of GKAP enhances the phase separation of the PSD assemblies

Each SAPAP protein contains multiple GBRs with SAPAP1 containing 5 repeats, SAPAP2 and SAPAP4 each containing 3 repeats, and SAPAP3 with 2 repeats (Figure 2A). The degree of SAPAP phosphorylation may correlate with the level and duration of CaMKII activation in synapses. Additionally, phase separation of biomolecular condensates is intimately linked to the valency of the molecular network of the condensates.[62] We next investigated whether the degree of GKAP phosphorylation is linked to the level of the condensate formation of the reconstituted PSD assembly. To address this question, each GKAP* protein with different GBRs phosphorylated (i.e., GKAP*-NP, -1P, -2P, or -3P) was mixed with four other PSD proteins (Stg, PSD-95, Shank3, and Homer1), and the resulting condensates were

compared and quantified. In this phase separation assay, the concentrations of PSD proteins and consequently the ratio of these proteins followed those quantified in earlier quantitative proteomic studies[63,64]: 5 μM Stg, 10 μM PSD-95, 3.3 μM GKAP*, 6.6 μM Shank3, and 6.6 μM Homer1. For totally unphosphorylated GKAP*, the resulting condensates contained two immiscible sub-compartments (Figure 4A, left panel; also see Figure 3A for an enlarged view). The PSD mixtures containing each of the three phosphorylated forms of GKAP* (GKAP*-1P, -2P, and -3P) formed homogeneous condensates, with signals from Stg, PSD-95, and Shanks completely overlapped with one another (Figure 4A, right three panels). Importantly, the degree of the condensate formation positively correlated with the number of GBRs phosphorylated in GKAP* (Figures 4A and 4B). We also performed a centrifugation-based phase separation experiment to quantify the condensate enrichments of each PSD protein. The assay result again showed that the enrichments of Stg and PSD-95 within the PSD assembly are positively correlated with the number of GBR phosphorylation sites of GKAP* (Figures 4C and 4D). These observations correlate well with previous findings showing that activation of CaMKIIα leads to structural long-term potentiation (LTP) with enlargements of PSD sizes and increased numbers of AMPARs in synapses.[65–70] It is noted that Stg is not a direct binder of GKAP, but the modifications on GKAP can remotely and robustly affect Stg to be enriched in the reconstituted condensates. The results from our phase separation assays provide an explanation to why *Sapap* knockout mice display downregulated transmission of AMPARs in synapses.[71–73]

PSDs are tethered to the postsynaptic plasma membranes for anchoring glutamate receptors, ion channels, and synaptic adhesion molecules. We therefore questioned whether phosphorylation of GBRs in GKAP might also change the PSD assembly phase separation on membrane surface by using the supported lipid bilayers (SLBs).[18,19] To mimic the membrane attachments of Stg and PSD-95 in native proteins, both Stg and PSD-95 were tagged at their N termini with a poly-His tag, which allows their tethering to SLBs containing DGS-NTA-Ni^{2+}. PSD-95 is considerably more abundant than Stg in PSDs.[64] To mimic the physiological relevant stoichiometry of the two proteins, the SLB was first coated with 2 μM His$_8$-PSD-95 for 1 h. After washing, His$_6$-Stg (0.05 μM), Shank3, Homer1, as well as GKAP* (each at 0.5 μM) with different numbers of GBRs phosphorylated were introduced to the SLBs to trigger phase separation (Figure 4E). Under this assay condition, GKAP*

(B) Fluorescence intensity line plots showing that iFluor-488-labeled PSD-95 and Alexa-647-labled Shank3 were localized into two distinct sub-compartments in (A).

(C) DIC/fluorescence microscopy images of homogeneous single-phase condensates formed by 10 μM Stg, PSD-95, GKAP*-1P, Shank3, and Homer1. (A) and (C) have the same scale.

(D) Fluorescence intensity line plots showing that iFluor-488-labeled PSD-95 and Alexa 647-labled Shank3 were co-localized in the same condensates in (C).

(E) Quantification of co-localization of two sub-compartments in GKAP*-NP and GKAP*-1P groups in (A) and (C). Error bars indicate ± SD. **p < 0.01. Student's t test.

(F and G) (Left) Mean square displacement (MSD) curves showing that both PSD-95 (F) and Shank3 (G) diffused slower when GKAP was phosphorylated. Data were plotted with mean value of MSD with standard error. Results for PSD-95 under the GKAP*-NP or GKAP*-1P conditions were derived using 1,740 and 3,664 tracks, respectively. Results for Shank under the GKAP*-NP and GKAP*-1P conditions were derived from 6,960 and 5,046 tracks, respectively. (Right) The diffusion coefficients of PSD-95 (F) and Shank3 (G) derived by fitting MSDs against time, using linear regression (MSD = 4Dt), where (D) is the diffusion coeeficient and t is the time duration. The apparent diffusion coefficient of each protein under any given condition was derived from measurements of four different regions in condensates. Data were expressed as mean ± SD with ****p < 0.0001 and ***p < 0.001. Student's t test.

(H) Time-lapse images showing that adding 1 μM PP2A into homogeneous single-phase condensates formed by 10 μM Stg, PSD-95, GKAP*-1P, Shank3, and Homer1 led to the fission of the condensate into two immiscible sub-compartments, i.e., PSD-95 sub-compartment and Shank3 sub-compartment.
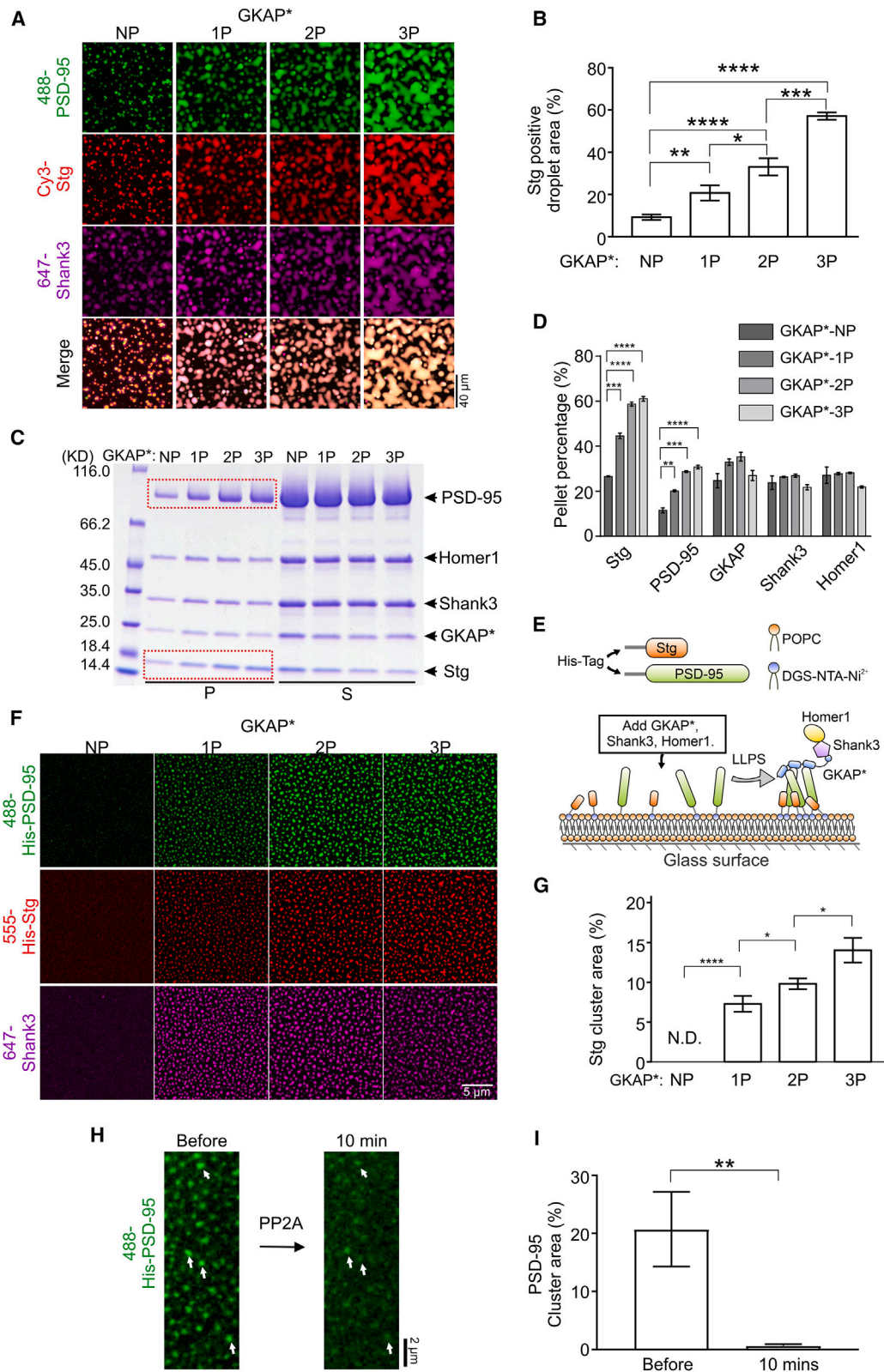
without any phosphorylation was incapable of inducing the clustering of PSD proteins on the membrane surface (i.e., the PSD proteins have not reached their threshold concentrations under the assay condition). The clustering of the PSD proteins, including Stg, PSD-95, and Shank3, progressively increased with the increases of the sites of GBR phosphorylation in GKAP* (Figures 4F and 4G). Consistent with the finding in Figure 3H, protein clusters on the membrane could be dispersed upon addition of 1 μM PP2A (Figures 4H and 4I). Taking all the above data together, we concluded that phosphorylation and dephosphorylation of GKAP can dynamically regulate the assembly of fusion and fission of condensates formed by the reconstituted PSD mixtures, and the level of GKAP phosphorylation determines the degree of PSD assembly formation and Stg clustering.

A designed GKAP-DLS protein mimicking constitutively phosphorylated GKAP

We next wanted to investigate whether phosphorylation of GBRs on GKAP is directly correlated with the synapse development and brain functions in living neurons. However, directly studying stoichiometric GKAP phosphorylation in living neurons is challenging due to intrinsic dynamic phosphorylation levels of the protein. Additionally, we showed that replacing the CaMKII targeting Ser in GKAP GBRs with Glu cannot mimic GBR phosphorylation.[51] Instead, a designed peptide derived from GBR2 of GKAP ("RIR-REE$_0$YRRAINGQSFDLS," where the sequence underlined represents the optimized GBR2 with the CaMKII targeting Ser at the position 0 replaced by Glu, and the peptide is named "DLS-SE") was shown to be a strong and specific binder of PSD-95.[51] Replacing Glu at the position 0 of the DLS-SE with Ala completely abolished the peptide's binding to PSD-95.[51] Thus, the DLS-SE peptide may mimic the constitutively phosphorylated GKAP GBR in binding to PSD-95, and the DLS-SA mutant peptide can act as a negative control of the DLS-SE peptide. We then examined whether substitutions of GBRs on GKAP with the DLS-SE peptide could mimic the GKAP phosphorylation with *in vitro* biochemical experiments. We replaced either one GBR (1×DLS-SE) or all three GBRs (3×

DLS-SE) of GKAP with the DLS-SE peptide to mimic a low and a high level of GKAP phosphorylation, respectively. Designed GKAP containing 1× or 3×DLS-SA was used as the negative control (Figure 5A). ITC-based binding measurements confirmed that GKAP-1×DLS-SE binds to PSD-95 with a K_D value of 1.7 μM (Figure 5B), which is quite strong even though still somewhat weaker than that of GKAP*-1P binding to PSD-95 ($K_D \sim 0.2$ μM) (Figure 2H). As expected, the GKAP-1×DLS-SA had no detectable binding to PSD-95 (Figure 5B).

In the phase separation assay for the PSD assembly with GKAP WT replaced by the designed GKAP proteins, the condensates containing GKAP-1×DLS-SE showed coalesced PSD-95 droplets with the Shank3 droplets (Figure 5C). In contrast, in the condensate containing GKAP-1×DLS-SA, the PSD-95/Stg droplets were segregated from the Shank3 droplets (Figure 5C). The condensates containing GKAP-3×DLS-SE were much more robust than the condensates containing GKAP-3× DLS-SA in confocal imaging assays (Figures 5D and 5E). Centrifugation-based phase separation assay showed that GKAP-3× DLS specifically enhanced the enrichments of PSD-95 and Stg in the condensed phase (Figures 5F and 5G). Lastly, we also performed phase separation assays on SLBs and the result showed that GKAP-3×DLS-SE, but not GKAP-3×DLS-SA, could efficiently cluster PSD proteins on the membrane surface (Figures 5H and 5I). Thus, the designed GKAP-3×DLS-SE and GKAP-3×DLS-SA proteins can be used to mimic constitutively phosphorylated and unphosphorylated forms of GKAP, respectively, for subsequent functional studies in probing roles of GKAP GBR phosphorylation in neurons in culture and in mice.

Phosphorylation of GBRs of SAPAPs is critical for synaptic development in cultured neurons

For functional assays, we replaced the first three GBRs of the full-length SAPAP1 with the DLS-SE or DLS-SA sequences (two constructs were denoted as SAPAP1-3×DLS-SE and SAPAP1-3× DLS-SA) (Figure 6A). To avoid introducing too many foreign amino acid residues to the designed SAPAP1, we did not replace GBR4

Figure 4. Phosphorylation of multiple GBRs enhances phase separation of PSD proteins

(A) Confocal images showing the phase separation of 5 PSD proteins, including Stg (Cy3-labeled), PSD-95 (iFluor-488-labeled), Shank3 (Alexa 647-labeled), Homer1, and differentially phosphorylated GKAP*s (GKAP*-NP, GKAP*-1P, GKAP*-2P, and GKAP*-3P), in solution; protein concentrations are specified in the main text.

(B) Quantification of imaging data in (A) showing the phase separation capability of Stg is positively correlated with the phosphorylation level of GKAP*. Three independent batches of imaging were performed for each group for quantification. Error bars indicate ± SD. *p < 0.05, **p < 0.01, ***p < 0.001, and ****p < 0.0001, using one-way ANOVA with Tukey's multiple comparison test.

(C) Representative SDS-PAGE showing the distributions of Stg, PSD-95, GKAP*, Shank3, and Homer1 recovered in the dilute phase/supernatant (S) and the condensed phase/pellet (P).

(D) Quantification of data in (C). Results were from 3 independent batches of sedimentation assays and are presented as mean ± SD. **p < 0.01, ***p < 0.001, and ****p < 0.0001, using one-way ANOVA with Tukey's multiple comparison test.

(E) Schematic diagram showing the PSD assembly formation via phase separation and Stg/PSD-95 clustering on SLBs.

(F) Confocal images showing the phase separation of 5 PSD components, including His$_6$-Stg (iFluor-555-labeled), His$_8$-PSD-95 (iFluor-488-labeled), Shank3 (Alexa 647-labeled), Homer1, and differentially phosphorylated GKAP*s (GKAP*-NP, GKAP*-1P, GKAP*-2P, and GKAP*-3P), on supported lipid membrane bilayers. The concentration of Shank3, Homer1, and GKAP*s added at 500 nM.

(G) Quantification of image data in (F) showing the surface clustering of Stg is positively correlated with the phosphorylation level on GKAP*. Results were from 3 independent batches of imaging assays and are presented as mean ± SD. *p < 0.05, ***p < 0.001, and ****p < 0.0001, using one-way ANOVA with Tukey's multiple comparison test.

(H) Time-lapse imaging by total internal reflection fluorescence (TIRF) microscope showing that adding 1 μM PP2A into preformed PSD clusters by His$_8$-PSD-95 (iFluor-488-labeled), His$_6$-Stg, GKAP*-1P, Shank3, and Homer1 on SLBs led to dispersion of the PSD-95 clusters. The arrows highlight the shrinking or even near disappearance of several prominent PSD-95 clusters by PP2A.

(I) Quantification of image data in (H) showing the dispersion of His$_8$-PSD-95 clusters on SLBs, mean ± SD, **p < 0.01, Student's t-test.
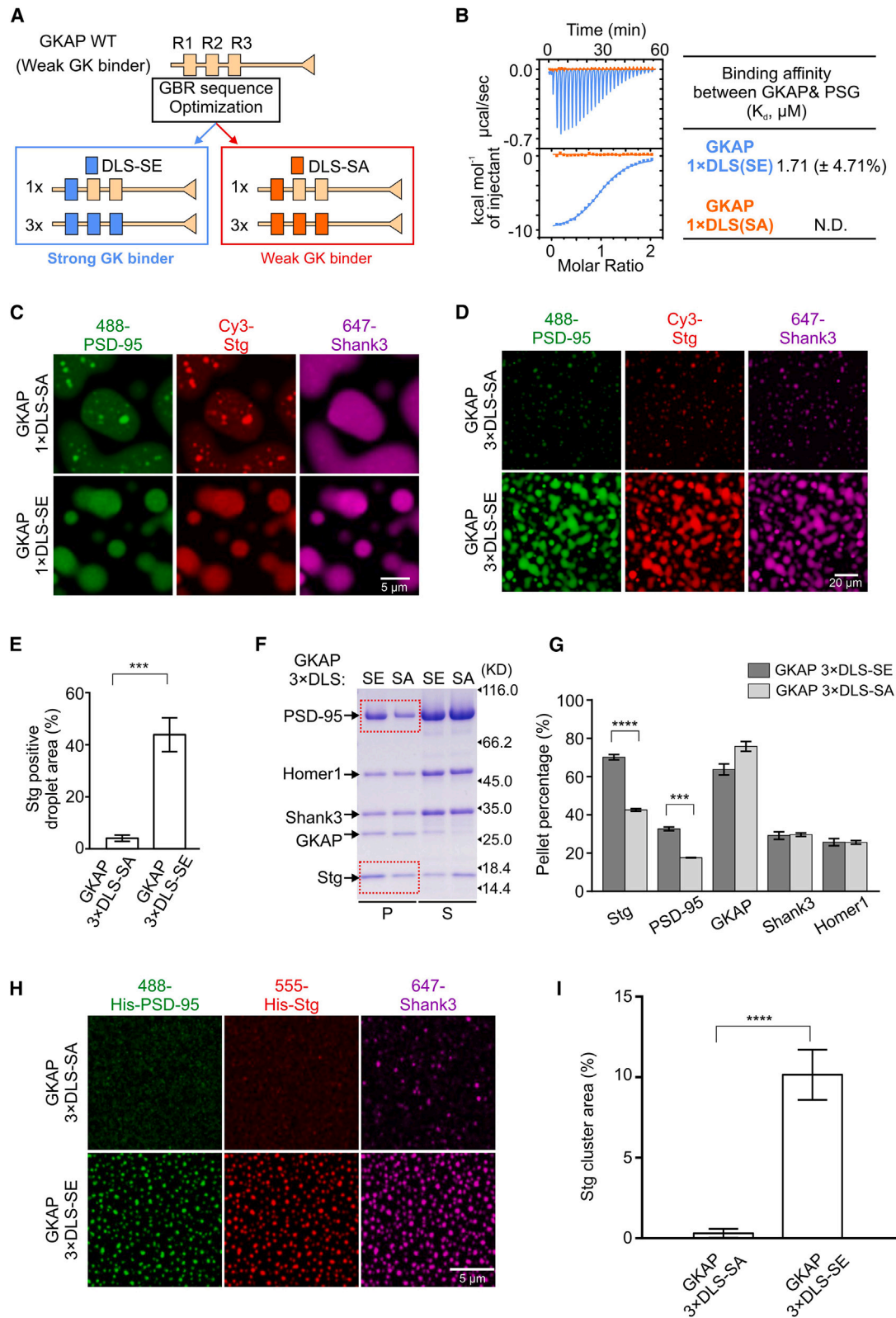
and GBR5 with the designed peptide sequence. Instead, the CaM-KII-targeting Ser in GBR 4 and GBR 5 of the protein were replaced with Ala to silence its phosphorylation by CaMKII (Figure 6A). GFP-SAPAP1-3×DLS-SE (served as a PSD phase separation enhancer), 3×DLS-SA (served as a PSD phase separation inhibitor), GFP-SAPAP1 WT (the positive control), and GFP (the background control) were individually co-expressed with mCherry (as a cell filler) in cultured hippocampal neurons during days in vitro (DIV) 14–17. The expression of GFP-SAPAP1 WT led to a prominent increase of spine size (as indicated by spine head width), when compared with the background control group expressing GFP only (Figures 6B and 6C). Strikingly, GFP-SAPAP1-3×DLS-SE also induced the maturation of dendritic spine to nearly the same level as GFP-SAPAP1 WT did, whereas no spine enlargement was observed in the neurons expressing GFP-SAPAP1-3×DLS-SA (Figures 6B and 6C). Hence, we concluded that the phosphorylation of GBRs of SAPAP1 is essential for the spine development mediated by SAPAP1, likely as a result of enhanced PSD-95/SAPAP1 interaction and subsequent promotion of PSD assembly formation.

All SAPAP family proteins contain various repeats of GBR (Figure 2A). We hypothesized that the phosphorylation-induced GBR/PSD-95 interaction is a conserved regulatory mechanism among all the SAPAPs. To generalize this mechanism and to set up the necessary in vitro mechanistic control for the in vivo study below, we also probed the synaptic functions of SAPAP3 in cultured neurons by replacing both GBRs on SAPAP3 with 2×DLS-SE or with 2×DLS-SA (denoted as GFP-SAPAP3-2×DLS-SE and GFP-SAPAP3-2×DLS-SA) (Figure 6D). Consistent with our previous findings, expression of GFP-SAPAP3 WT promoted the spine enlargement[51] (Figures 6E and 6F). As expected, GFP-SAPAP3-2×DLS-SE, but not GFP-SAPAP3-2×DLS-SA, could promote enlargement of spine head when expressed in neurons (Figures 6E and 6F).

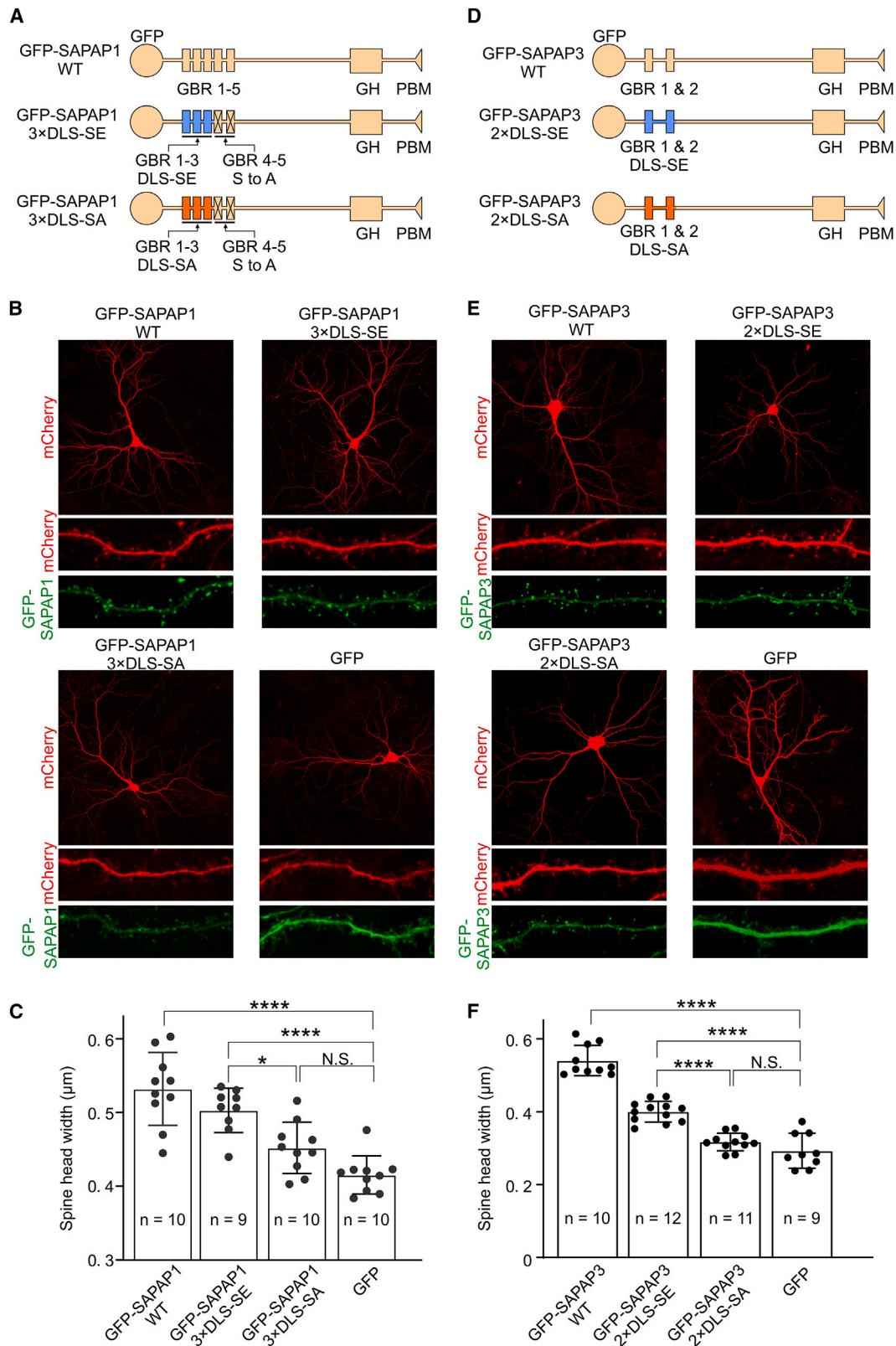### Blocking SAPAP3 phosphorylation leads to increased separation of PSD-95 and Homer1 in synapses of striatum neurons

We next asked whether blocking SAPAP phosphorylation in neurons in vivo could prevent the fusion of the upper and lower layers of the two PSD sub-compartments. It is known that SAPAP3 is the dominant SAPAP isoform expressed in striatum in the mice brain, whereas other brain regions typically simultaneously express several isoforms of SAPAP proteins.[73,74] Thus, neurons in mice striatum are an ideal system for assaying roles of SAPAP phosphorylation on PSD formation by replacing the endogenous SAPAP3 with the SAPAP3 mutants characterized in cultured neurons in Figures 6E and 6F. To achieve this goal, we generated Sapap3 knockout mice (Figures S3A–3C). The Sapap3$^{-/-}$ mice displayed typical obsessive-compulsive disorder phenotype as manifested by over-grooming that caused facial lesions (Figures 3E and S3D).[73,75–77] We then expressed various forms of SAPAP3 mutants in striatum of Sapap3$^{-/-}$ mice using an adeno-associated virus (AAV)-mediated gene delivery approach. The deletion of endogenous SAPAP3 protein in whole brain of Sapap3$^{-/-}$ mice was confirmed by western blot using a SAPAP3 antibody (Figure S3C), and the expression of exogenous SAPAP3 in the striatum of Sapap3$^{-/-}$ mice was visualized by immunostaining the FLAG tag fused to the N terminus of SAPAP3 (Figure S3F).

We then assayed the distributions of key synaptic proteins (PSD-95 as the top-layer PSD marker and Homer1 as the lower-layer PSD marker) in brain slices of these SAPAP3 variant-expressing mice using stochastic optical reconstruction microscopy (STORM)-based super-resolution imaging experiments (Figure 7A). The localizations of PSD-95 and Homer1 molecules in each PSD were projected along the trans-PSD axis that is perpendicular to the fitted planes of the PSD-95 and Homer1 localizations (Figure 7B, top panel). The distance between the peak positions of PSD-95 and Homer1 distributions was defined as the distance between PSD-95 and Homer1 in each synapse (Figure 7B). We observed that re-expression of SAPAP3 WT in the striatum of Sapap3$^{-/-}$ mice could effectively narrow the distance between PSD-95 and Homer1 from ~50 to ~35 nm (Figure 7C). The distance of ~35 nm between PSD-95 and Homer1 in SAPAP3 WT-expressing mice is highly consistent with the value reported by an earlier study[78] using the same STORM-imaging and analysis methods. Importantly, the constitutive SAPAP3 phosphorylation mutant (SAPAP3 2×DLS-SE) could also narrow the distribution distance of PSD-95 and Homer1 to ~35 nm, whereas the phosphorylation-defective mutants (SAPAP3 2×DLS-SA and SAPAP3 S2A) could not narrow the

---

Figure 5. A designed GKAP-DLS protein mimicking constitutively phosphorylated GKAP

(A) Schematic diagram showing the designs of GKAP-DLS to constitutively mimic phosphorylated GKAPs.

(B) ITC measurements showing that GKAP 1×DLS-SE strongly interacts with PSD-95 PSG (blue curve), but GKAP 1×DLS-SA does not (orange curve). 200 μM GKAP 1×DLS-SE or -SA was titrated to 20 μM PSG.

(C) Confocal imaging showing the phase separation of 5 PSD components, including Stg (Cy3-labeled), PSD-95 (iFluor-488-labeled), Shank3 (Alexa 647-labeled), Homer1, and GKAP 1×DLS-SE or -SA, respectively. PSD-95 and Stg formed immiscible sub-compartment with the Shank3/Homer sub-compartment in the 1× DLS-SA group but not in the 1×DLS-SE group. All proteins were at 5 μM concentration.

(D) Confocal imaging showing the phase separation of 5 PSD components, including Stg (Cy3-labeled), PSD-95 (iFluor-488-labeled), Shank3 (Alexa-647-labeled), Homer1, and GKAP 3×DLS-SE or -SA, respectively. All proteins were in 5 μM concentration.

(E) Quantification of image data in (D) showing the phase separation capability of Stg in the 3×DLS-SE group was much stronger than in the 3×DLS-SA group. Results were from 3 independent batches and are presented as mean ± SD, ***p < 0.001. Student's t test.

(F) Representative SDS-PAGE showing the distributions of Stg, PSD-95, GKAP (3×DLS-SE or -SA), Shank3, and Homer1 recovered in the dilute phase/supernatant (S) and condensed phase/pellet (P). All proteins were in 5 μM concentration.

(G) Quantification of data in (F) showing Stg and PSD-95 were more enriched in the condensed phase when using GKAP 3×DLS-SE. Results were from 3 independent batches of sedimentation assays and are presented as mean ± SD. ***p < 0.001 and ****p < 0.0001. Student's t test.

(H) Confocal imaging showing the phase separation of 5 PSD components, including His$_6$-Stg (iFluor-555-labeled), His$_8$-PSD-95 (iFluor-488-labeled), Shank3 (Alexa 647-labeled), Homer1, and GKAP (3×DLS-SE or -SA), on SLBs. Shank3, Homer1, and two GKAPs were added at 100 nM.

(I) Quantification of imaging data in (H) showing GKAP 3×DLS-SE is more capable of clustering Stg, PSD-95, and Shank3 on the SLBs. Results were from 3 independent batches of imaging assays and are presented as mean ± SD. ****p < 0.0001. Student's t test.

A

GFP-SAPAP1 WT

GFP-SAPAP1 3×DLS-SE

GFP-SAPAP1 3×DLS-SA

D

GFP-SAPAP3 WT

GFP-SAPAP3 2×DLS-SE

GFP-SAPAP3 2×DLS-SA

B

GFP-SAPAP1 WT — GFP-SAPAP1 3×DLS-SE — GFP-SAPAP1 3×DLS-SA — GFP

E

GFP-SAPAP3 WT — GFP-SAPAP3 2×DLS-SE — GFP-SAPAP3 2×DLS-SA — GFP

C

Spine head width (μm)

n = 10, n = 9, n = 10, n = 10

GFP-SAPAP1 WT, GFP-SAPAP1 3×DLS-SE, GFP-SAPAP1 3×DLS-SA, GFP

F

Spine head width (μm)

n = 10, n = 12, n = 11, n = 9

GFP-SAPAP3 WT, GFP-SAPAP3 2×DLS-SE, GFP-SAPAP3 2×DLS-SA, GFP

(legend on next page)

gap between PSD-95 and Homer1 induced by the *Sapap*3 knockout (Figure 7C). The above super-resolution imaging experiments provide *in vivo* evidence showing that phosphorylation of SAPAP3 is required for the dynamic distributions of the PSD scaffold proteins in synapses. Since PSD-95 is palmitoylated and thus constitutively attached to the plasma membranes of PSDs,[79] the phosphorylation-induced narrowing of the distance between PSD-95 and Homer1 may be interpreted as shifting of Homer1 toward PSD-95, an event consistent with SAPAP3 phosphorylation-induced fusion of the lower-layer PSD sub-compartment with the upper-layer PSD sub-compartment.

DISCUSSION

In this study, we demonstrate that the PSD assembly reconstituted *in vitro* with unphosphorylated proteins exists as two immiscible sub-compartments corresponding to the membrane proximal layer and membrane distal layer via phase separation. These two sub-compartments are linked by SAPAP, one of the PSD scaffold proteins that can bind to proteins in both sub-compartments. Thus, the two sub-compartments are organized in a phase-in-phase pattern with the unphosphorylated SAPAP as the tether of the two phases. Phosphorylation of SAPAP leads to fusion of the two sub-compartments into a single condensate, accompanied with increased enrichment of PSD-95 and Stg in the condensate. Dephosphorylation of SAPAP caused the single phase of the PSD assembly fission into two sub-compartments corresponding to the upper-layer and lower-layer PSD sub-compartments (see Figure 7D for a model). Super-resolution imaging studies show that blocking SAPAP phosphorylation prevents shifting of the lower-layer scaffold protein Homer1 toward the core of PSD in synapses of mice brain. The above observation suggests that membraneless organelles formed via phase separation (e.g., the PSD assembly studied here), analogous to membrane-based organelles, can undergo regulated fusion and fission. Such regulated membraneless organelle fusion and fission, if existing broadly in cells, may have profound implications on cellular functions exerted by membraneless organelles via regulating their formation/dissolution, composition, activity, material property, cellular localization, etc. It should be noted that the molecular mechanisms underlying fusion and fission of membraneless organelles and membrane organelles are totally different. Fusion and fission of membrane organelles involve membrane fusion and fission and require SNARE protein machineries.[80,81] In contrast, fusion and fission of membraneless organelles do not require SNAREs and can occur facilely by modulating molecular interactions between two sub-organelles.

Our findings on the SAPAP phosphorylation-regulated condensate fusion and growth provide a mechanistic explanation to the activity-dependent PSD assembly growth (also referred to as sLTP) of synapses (Figure 7D). When CaMKII or other relevant kinase activity is low, the Ser residues in the GBR repeats of SAPAPs are largely unphosphorylated due to actions of phosphatases in synapses.[60] Under such condition, synapses are generally small in volume and low in electric activity, and their PSDs exist as two distinct sub-compartments, corresponding to the PSD core and pallium observed in EM-based studies.[27] The sub-compartment right beneath the synaptic plasma membrane (or the PSD core) contains glutamate receptors and PSD-95, and the lower layer of PSD (or the PSD pallium) contains scaffold proteins such as Shank and Homer. Synaptic activity-induced Ca^{2+} influx activates CaMKII or other kinases, and subsequent phosphorylation of SAPAP leads to fusion of the two PSD sub-compartments and increased enrichment/clustering of Stg (and therefor AMPARs) in the PSD, resulting in synapse maturation. Sustained kinase activation can result in accumulated phosphorylation of Ser residues in multiple GBRs of SAPAPs. Such high-level SAPAP phosphorylation leads to further expansion of the PSD assembly, accompanied with further increase of the Stg (and AMPARs) density within the PSD, a process that matches well with the extensively documented synaptic spine and PSD enlargements under LTP conditions.[65–70] It should be noted that processes other than SAPAP phosphorylation studied here may also participate in the enlargement or shrinking of the PSD. It is known that events such as protein synthesis/turnover, protein trafficking, actin cytoskeletal dynamic changes, etc. are closely related to PSD size and consequently synapse volume changes.[39–45,82] These processes may work with SAPAP phosphorylation or function independently in regulating PSD dynamics and synaptic plasticity.

Limitations of the study

The SAPAP phosphorylation-dependent fusion and fission of the partially reconstituted PSD condensates demonstrated in this study are based on an *in vitro* reconstitution system. In this study, we had to use truncated Shank3, SAPAP1, and the cytoplasmic tail of Stg for our reconstitution study, as such truncated proteins could be produced and purified with high homogeneity for phase separation studies. Although our studies using the *Sapap3* knockout mice provided *in vivo* evidence supporting SAPAP3 phosphorylation-dependent shifting of the lower-layer PSD scaffold proteins toward the postsynaptic membrane-tethered PSD core, these super-resolution imaging results do not directly demonstrate that in synapses of living neurons, the two layers of the PSD scaffold proteins form condensates via

Figure 6. Phosphorylation of GBRs of SAPAPs is critical for synapse maturation in cultured neurons
(A) Schematic diagram showing GFP-SAPAP1 WT, GFP-SAPAP1 3×DLS-SE, and GFP-SAPAP1 3×DLS-SA constructs designed for synapse maturation assay in primary neuron cultures.
(B) Imaging data showing dendritic spines in hippocampal neurons expressing GFP-SAPAP1 WT, GFP-SAPAP1 3×DLS-SE, GFP-SAPAP1 3×DLS-SA, and GFP.
(C) Quantification of spine head width of imaging data in (B). Error bar indicates ± SD. ****p < 0.0001, *p < 0.05, and NS, not significant. One-way ANOVA with Tukey's multiple comparison test was used. n stands for number of neurons compiled from three different batches of cultures.
(D) Schematic diagram showing GFP-SAPAP3 WT, GFP-SAPAP3 2×DLS-SE, and GFP-SAPAP3 2×DLS-SA constructs designed for synapse maturation assay in primary neuron cultures.
(E) Imaging data showing dendritic spines in neurons expressing GFP-SAPAP3 WT, GFP-SAPAP3 2×DLS-SE, GFP-SAPAP3 2×DLS-SA, and GFP.
(F) Quantification of spine head width in imaging data in (E). Error bar indicates ± SD. ****p < 0.0001 and NS, not significant. One-way ANOVA with Tukey's multiple comparison test was used. n stands for number of neurons compiled from three different batches of cultures.
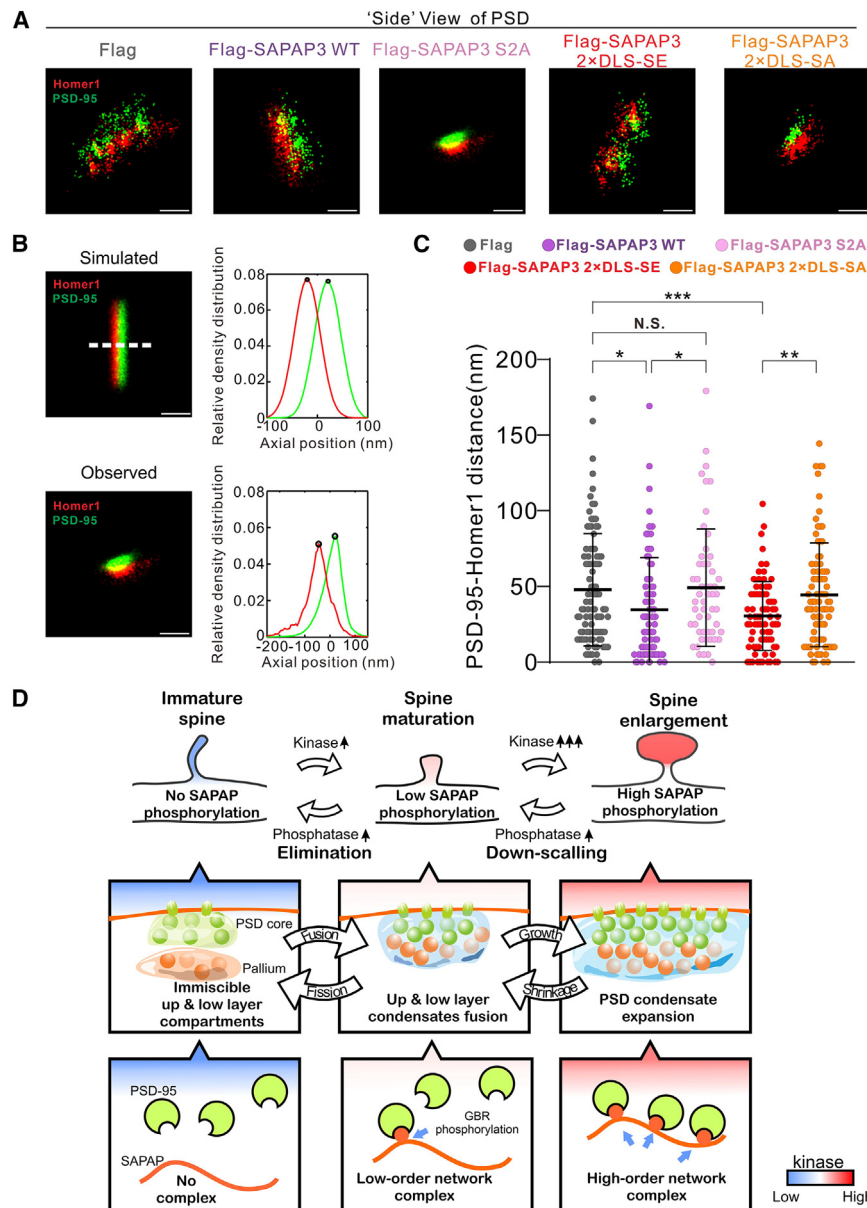
Figure 7. Distributions of PSD-95 and Homer1 in synapses of striatum neurons of mice expressing different SAPAP3 variants

(A) Representative STORM images of PSDs of striatum neuronal synapses from *Sapap3*$^{-/-}$ mice brain slices expressing different rescuing SAPAP3 variants. PSD-95 and Homer1 signals are shown in green and red, respectively. Scale bars: 200 nm.

(B) Upper left panel shows the side view of simulated PSD-95 and Homer signals in a synapse that has ideal Gaussian distributions alone; the PSD axis is indicated with a white dashed line. Bottom left panel shows the side view of PSD-95 and Homer1 signals from a PSD-expressing "FLAG-SAPAP3 S2A." Upper and bottom right panels show the corresponding density distribution profiles of PSD-95 and Homer1 along the PSD axis. Scale bars, 200 nm.

(C) Statistics analysis of the distances between PSD-95 and Homer1 among the groups as in (A). Each dot was calculated from one PSD. We selected 94 PSDs in the FLAG control, 77 PSDs in FLAG-SAPAP3 WT, 54 PSDs in FLAG-SAPAP3 S2A, 77 PSDs in FLAG-SAPAP3 2×DLS-SE, and 86 PSDs in FLAG-SAPAP3 2×DLS-SA for the quantification. Each group of data was obtained from two different brain slices. Data were presented as dots, and the mean value for each group is indicated by a black bar. Error bar indicates ± SD. *p < 0.05, **p < 0.01, and ***p < 0.001. Student's t test.

(D) A model depicting the bidirectional regulation of PSD fission and fusion by phosphorylation of SAPAP. Increased SAPAP phosphorylation leads to enhanced PSD assembly formation via fusion of the PSD core and pallium sub-compartments and consequently enlarged PSD size and more mature dendritic spines.

phase separation, and the condensates undergo phosphorylation-dependent fusion and fission. Such limitation is imposed by the size of the PSD, which makes it extremely challenging to directly observe phase separation events using currently available optical imaging technologies. Thus, future studies are required to directly demonstrate that regulated fusion and fission events such as the PSD assemblies shown in this *in vitro* study indeed occur in neuronal synapses or in other living cell systems.

STAR★METHODS

Detailed methods are provided in the online version of this paper and include the following:

- KEY RESOURCES TABLE
- RESOURCE AVAILABILITY
  - ○ Lead contact
  - ○ Materials availability
  - ○ Data and code availability
- EXPERIMENTAL MODEL AND STUDY PARTICIPANT DETAILS
  - ○ Primary hippocampal neuron culture
  - ○ Mice
- METHOD DETAILS
  - ○ Protein expression and purification
  - ○ Protein fluorescence labeling
  - ○ Imaging-based assay of phase separation
  - ○ CaMKIIα auto-phosphorylation
  - ○ GKAP/GKAP* *in vitro* phosphorylation
  - ○ Phos-Tag™ SDS-PAGE
  - ○ Lipid bilayer preparation and phase separation assay
  - ○ Isothermal titration calorimetry assay

- ○ Fast protein liquid chromatography coupled with static light scattering
  - ○ Single molecule tracking for 3D phase separation system
  - ○ Behavioral analysis
  - ○ Stereotaxic injection
  - ○ Immunohistochemistry
  - ○ Western blot
  - ○ dSTORM image acquisition
- ● QUANTIFICATION AND STATISTICAL ANALYSIS
  - ○ Quantification of colocalization
  - ○ Quantification of cluster area in SLBs
  - ○ Quantification of dSTORM imaging for brain slice

SUPPLEMENTAL INFORMATION

Supplemental information can be found online at https://doi.org/10.1016/j.molcel.2023.11.011.

AUTHOR CONTRIBUTIONS

H.W., X.C., and M.Z. conceived the idea and designed the experiments; H.W., X.C., Z.S., and S.L. performed experiments and analyzed data; H.L., S.L., and Y.L. contributed to the mice experiments; X.C., H.W., Z.S., and M.Z. wrote and revised the manuscript, and all authors provided input; M.Z. coordinated the study.

DECLARATION OF INTERESTS

The authors declare no competing interests.

REFERENCES

1. Brangwynne, C.P., Eckmann, C.R., Courson, D.S., Rybarska, A., Hoege, C., Gharakhani, J., Jülicher, F., and Hyman, A.A. (2009). Germline P granules are liquid droplets that localize by controlled dissolution/condensation. Science *324*, 1729–1732.

2. Banani, S.F., Lee, H.O., Hyman, A.A., and Rosen, M.K. (2017). Biomolecular condensates: organizers of cellular biochemistry. Nat. Rev. Mol. Cell Biol. *18*, 285–298.

3. Chen, X., Wu, X., Wu, H., and Zhang, M. (2020). Phase separation at the synapse. Nat. Neurosci. *23*, 301–310.

4. Hyman, A.A., Weber, C.A., and Jülicher, F. (2014). Liquid-liquid phase separation in biology. Annu. Rev. Cell Dev. Biol. *30*, 39–58.

5. Wu, X., Cai, Q., Feng, Z., and Zhang, M. (2020). Liquid-liquid phase separation in neuronal development and synaptic signaling. Dev. Cell *55*, 18–29.

6. Lyon, A.S., Peeples, W.B., and Rosen, M.K. (2021). A framework for understanding the functions of biomolecular condensates across scales. Nat. Rev. Mol. Cell Biol. *22*, 215–235.

7. Shin, Y., Berry, J., Pannucci, N., Haataja, M.P., Toettcher, J.E., and Brangwynne, C.P. (2017). Spatiotemporal control of intracellular phase transitions using light-activated optoDroplets. Cell *168*, 159–171.e14.

8. Bhat, P., Honson, D., and Guttman, M. (2021). Nuclear compartmentalization as a mechanism of quantitative control of gene expression. Nat. Rev. Mol. Cell Biol. *22*, 653–670.

9. Ong, J.Y., and Torres, J.Z. (2020). Phase separation in cell division. Mol. Cell *80*, 9–20.

10. Su, Q., Mehta, S., and Zhang, J. (2021). Liquid-liquid phase separation: orchestrating cell signaling through time and space. Mol. Cell *81*, 4137–4146.

11. Noda, N.N., Wang, Z., and Zhang, H. (2020). Liquid-liquid phase separation in autophagy. J. Cell Biol. *219*, e202004062.

12. Xiao, Q., McAtee, C.K., and Su, X. (2022). Phase separation in immune signalling. Nat. Rev. Immunol. *22*, 188–199.

13. Wu, X., Ganzella, M., Zhou, J., Zhu, S., Jahn, R., and Zhang, M. (2021). Vesicle tethering on the surface of phase-separated active zone condensates. Mol. Cell *81*, 13–24.e7.

14. Dignon, G.L., Best, R.B., and Mittal, J. (2020). Biomolecular phase separation: from molecular driving forces to macroscopic properties. Annu. Rev. Phys. Chem. *71*, 53–75.

15. Fare, C.M., Villani, A., Drake, L.E., and Shorter, J. (2021). Higher-order organization of biomolecular condensates. Open Biol. *11*, 210137.

16. Snead, W.T., and Gladfelter, A.S. (2019). The control centers of biomolecular phase separation: how membrane surfaces, PTMs, and active processes regulate condensation. Mol. Cell *76*, 295–305.

17. Zeng, M., Shang, Y., Araki, Y., Guo, T., Huganir, R.L., and Zhang, M. (2016). Phase transition in postsynaptic densities underlies formation of synaptic complexes and synaptic plasticity. Cell *166*, 1163–1175.e12.

18. Zeng, M., Chen, X., Guan, D., Xu, J., Wu, H., Tong, P., and Zhang, M. (2018). Reconstituted postsynaptic density as a molecular platform for understanding synapse formation and plasticity. Cell *174*, 1172–1187.e16.

19. Zeng, M., Díaz-Alonso, J., Ye, F., Chen, X., Xu, J., Ji, Z., Nicoll, R.A., and Zhang, M. (2019). Phase separation-mediated TARP/MAGUK complex condensation and AMPA receptor synaptic transmission. Neuron *104*, 529–543.e6.

20. Borczyk, M., Śliwińska, M.A., Caly, A., Bernas, T., and Radwanska, K. (2019). Neuronal plasticity affects correlation between the size of dendritic spine and its postsynaptic density. Sci. Rep. *9*, 1693.

21. Harris, K.M., and Weinberg, R.J. (2012). Ultrastructure of synapses in the mammalian brain. Cold Spring Harb. Perspect. Biol. *4*, a005587.

22. Matsuzaki, M., Honkura, N., Ellis-Davies, G.C., and Kasai, H. (2004). Structural basis of long-term potentiation in single dendritic spines. Nature *429*, 761–766.

23. Chen, X., Levy, J.M., Hou, A., Winters, C., Azzam, R., Sousa, A.A., Leapman, R.D., Nicoll, R.A., and Reese, T.S. (2015). PSD-95 family MAGUKs are essential for anchoring AMPA and NMDA receptor complexes at the postsynaptic density. Proc. Natl. Acad. Sci. USA *112*, E6983–E6992.

24. Matsuzaki, M., Ellis-Davies, G.C., Nemoto, T., Miyashita, Y., Iino, M., and Kasai, H. (2001). Dendritic spine geometry is critical for AMPA receptor expression in hippocampal CA1 pyramidal neurons. Nat. Neurosci. *4*, 1086–1092.

25. Harris, K.M., and Stevens, J.K. (1989). Dendritic spines of CA1 pyramidal cells in the rat hippocampus: serial electron microscopy with reference to their biophysical characteristics. J. Neurosci. *9*, 2982–2997.

26. Holler, S., Köstinger, G., Martin, K.A.C., Schuhknecht, G.F.P., and Stratford, K.J. (2021). Structure and function of a neocortical synapse. Nature *591*, 111–116.

27. Dosemeci, A., Weinberg, R.J., Reese, T.S., and Tao-Cheng, J.H. (2016). The postsynaptic density: there is more than meets the eye. Front. Synaptic Neurosci. *8*, 23.

28. Chen, X., Winters, C., Azzam, R., Li, X., Galbraith, J.A., Leapman, R.D., and Reese, T.S. (2008). Organization of the core structure of the postsynaptic density. Proc. Natl. Acad. Sci. USA *105*, 4453–4458.

29. Naisbitt, S., Kim, E., Tu, J.C., Xiao, B., Sala, C., Valtschanoff, J., Weinberg, R.J., Worley, P.F., and Sheng, M. (1999). Shank, a novel family of postsynaptic density proteins that binds to the NMDA receptor/PSD-95/GKAP complex and cortactin. Neuron *23*, 569–582.

30. Tu, J.C., Xiao, B., Naisbitt, S., Yuan, J.P., Petralia, R.S., Brakeman, P., Doan, A., Aakalu, V.K., Lanahan, A.A., Sheng, M., et al. (1999). Coupling of mGluR/Homer and PSD-95 complexes by the Shank family of postsynaptic density proteins. Neuron *23*, 583–592.

31. Xiao, B., Tu, J.C., Petralia, R.S., Yuan, J.P., Doan, A., Breder, C.D., Ruggiero, A., Lanahan, A.A., Wenthold, R.J., and Worley, P.F. (1998). Homer regulates the association of group 1 metabotropic glutamate receptors with multivalent complexes of homer-related, synaptic proteins. Neuron *21*, 707–716.

32. Tao-Cheng, J.H., Thein, S., Yang, Y., Reese, T.S., and Gallant, P.E. (2014). Homer is concentrated at the postsynaptic density and does not redistribute after acute synaptic stimulation. Neuroscience *266*, 80–90.

33. Naisbitt, S., Kim, E., Weinberg, R.J., Rao, A., Yang, F.C., Craig, A.M., and Sheng, M. (1997). Characterization of guanylate kinase-associated protein, a postsynaptic density protein at excitatory synapses that interacts directly with postsynaptic density-95/synapse-associated protein 90. J. Neurosci. *17*, 5687–5696.

34. Tao-Cheng, J.H., Yang, Y., Reese, T.S., and Dosemeci, A. (2015). Differential distribution of Shank and GKAP at the postsynaptic density. PLoS One *10*, e0118750.

35. Dosemeci, A., Tao-Cheng, J.H., Vinade, L., Winters, C.A., Pozzo-Miller, L., and Reese, T.S. (2001). Glutamate-induced transient modification of the postsynaptic density. Proc. Natl. Acad. Sci. USA *98*, 10428–10432.

36. Tao-Cheng, J.H. (2019). Stimulation induces gradual increases in the thickness and curvature of postsynaptic density of hippocampal CA1 neurons in slice cultures. Mol. Brain *12*, 44.

37. Fukunaga, Y., Nakajima, E., Hatano, E., Itoh, S., Kashino, Y., and Miyazawa, A. (2015). Activation of NMDA receptors thickens the postsynaptic density via proteolysis. Neurosci. Res. *101*, 6–14.

38. Sun, Y., Smirnov, M., Kamasawa, N., and Yasuda, R. (2021). Rapid ultrastructural changes in the PSD and surrounding membrane after induction of structural LTP in single dendritic spines. J. Neurosci. *41*, 7003–7014.

39. Ostroff, L.E., Fiala, J.C., Allwardt, B., and Harris, K.M. (2002). Polyribosomes redistribute from dendritic shafts into spines with enlarged synapses during LTP in developing rat hippocampal slices. Neuron *35*, 535–545.

40. Yang, Y., Wang, X.B., Frerking, M., and Zhou, Q. (2008). Spine expansion and stabilization associated with long-term potentiation. J. Neurosci. *28*, 5740–5751.

41. Tanaka, J., Horiike, Y., Matsuzaki, M., Miyazaki, T., Ellis-Davies, G.C., and Kasai, H. (2008). Protein synthesis and neurotrophin-dependent structural plasticity of single dendritic spines. Science *319*, 1683–1687.

42. Meyer, D., Bonhoeffer, T., and Scheuss, V. (2014). Balance and stability of synaptic structures during synaptic plasticity. Neuron *82*, 430–443.

43. Bosch, M., Castro, J., Saneyoshi, T., Matsuno, H., Sur, M., and Hayashi, Y. (2014). Structural and molecular remodeling of dendritic spine substructures during long-term potentiation. Neuron *82*, 444–459.

44. Chen, X., Jia, B., Araki, Y., Liu, B., Ye, F., Huganir, R., and Zhang, M. (2022). Arc weakens synapses by dispersing AMPA receptors from postsynaptic density via modulating PSD phase separation. Cell Res. *32*, 914–930.

45. Suzuki, T., Kametani, K., Guo, W., and Li, W. (2018). Protein components of post-synaptic density lattice, a backbone structure for type I excitatory synapses. J. Neurochem. *144*, 390–407.

46. Tao-Cheng, J.H. (2020). Activity-dependent redistribution of CaMKII in the postsynaptic compartment of hippocampal neurons. Mol. Brain *13*, 53.

47. Otmakhov, N., Tao-Cheng, J.H., Carpenter, S., Asrican, B., Dosemeci, A., Reese, T.S., and Lisman, J. (2004). Persistent accumulation of calcium/calmodulin-dependent protein kinase II in dendritic spines after induction of NMDA receptor-dependent chemical long-term potentiation. J. Neurosci. *24*, 9324–9331.

48. Murakoshi, H., Shin, M.E., Parra-Bueno, P., Szatmari, E.M., Shibata, A.C.E., and Yasuda, R. (2017). Kinetics of endogenous CaMKII required for synaptic plasticity revealed by optogenetic kinase inhibitor. Neuron *94*, 37–47.e5.

49. Malinow, R., Schulman, H., and Tsien, R.W. (1989). Inhibition of postsynaptic PKC or CaMKII blocks induction but not expression of LTP. Science *245*, 862–866.

50. Dosemeci, A., Vinade, L., Winters, C.A., Reese, T.S., and Tao-Cheng, J.H. (2002). Inhibition of phosphatase activity prolongs NMDA-induced modification of the postsynaptic density. J. Neurocytol. *31*, 605–612.

51. Zhu, J., Zhou, Q., Shang, Y., Li, H., Peng, M., Ke, X., Weng, Z., Zhang, R., Huang, X., Li, S.S.C., et al. (2017). Synaptic targeting and function of SAPAPs mediated by phosphorylation-dependent binding to PSD-95 MAGUKs. Cell Rep. *21*, 3781–3793.

52. Kim, E., Naisbitt, S., Hsueh, Y.P., Rao, A., Rothschild, A., Craig, A.M., and Sheng, M. (1997). GKAP, a novel synaptic protein that interacts with the guanylate kinase-like domain of the PSD-95/SAP90 family of channel clustering molecules. J. Cell Biol. *136*, 669–678.

53. Shin, S.M., Zhang, N., Hansen, J., Gerges, N.Z., Pak, D.T., Sheng, M., and Lee, S.H. (2012). GKAP orchestrates activity-dependent postsynaptic protein remodeling and homeostatic scaling. Nat. Neurosci. *15*, 1655–1666.

54. Zhu, J., Shang, Y., Xia, C., Wang, W., Wen, W., and Zhang, M. (2011). Guanylate kinase domains of the MAGUK family scaffold proteins as specific phospho-protein-binding modules. EMBO J. *30*, 4986–4997.

55. Johnston, C.A., Doe, C.Q., and Prehoda, K.E. (2012). Structure of an enzyme-derived phosphoprotein recognition domain. PLoS One *7*, e36014.

56. Zeng, M., Shang, Y., Guo, T., He, Q., Yung, W.H., Liu, K., and Zhang, M. (2016). A binding site outside the canonical PDZ domain determines the specific interaction between Shank and SAPAP and their function. Proc. Natl. Acad. Sci. USA *113*, E3081–E3090.

57. Shen, Z., Jia, B., Xu, Y., Wessén, J., Pal, T., Chan, H.S., Du, S., and Zhang, M. (2023). Biological condensates form percolated networks with molecular motion properties distinctly different from dilute solutions. eLife *12*, e81907.

58. Coba, M.P. (2019). Regulatory mechanisms in postsynaptic phosphorylation networks. Curr. Opin. Struct. Biol. *54*, 86–94.

59. Coba, M.P., Pocklington, A.J., Collins, M.O., Kopanitsa, M.V., Uren, R.T., Swamy, S., Croning, M.D., Choudhary, J.S., and Grant, S.G. (2009). Neurotransmitters drive combinatorial multistate postsynaptic density networks. Sci. Signal. *2*, ra19.

60. Cai, Q., Zeng, M., Wu, X., Wu, H., Zhan, Y., Tian, R., and Zhang, M. (2021). CaMKIIalpha-driven, phosphatase-checked postsynaptic plasticity via phase separation. Cell Res. *31*, 37–51.

61. Strack, S., Zaucha, J.A., Ebner, F.F., Colbran, R.J., and Wadzinski, B.E. (1998). Brain protein phosphatase 2A: developmental regulation and distinct cellular and subcellular localization by B subunits. J. Comp. Neurol. *392*, 515–527.

62. Li, P., Banjade, S., Cheng, H.C., Kim, S., Chen, B., Guo, L., Llaguno, M., Hollingsworth, J.V., King, D.S., Banani, S.F., et al. (2012). Phase transitions in the assembly of multivalent signalling proteins. Nature *483*, 336–340.

63. Sugiyama, Y., Kawabata, I., Sobue, K., and Okabe, S. (2005). Determination of absolute protein numbers in single synapses by a GFP-based calibration technique. Nat. Methods *2*, 677–684.

64. Cheng, D., Hoogenraad, C.C., Rush, J., Ramm, E., Schlager, M.A., Duong, D.M., Xu, P., Wijayawardana, S.R., Hanfelt, J., Nakagawa, T., et al. (2006). Relative and absolute quantification of postsynaptic density proteome isolated from rat forebrain and cerebellum. Mol. Cell. Proteomics *5*, 1158–1170.

65. Lisman, J., Yasuda, R., and Raghavachari, S. (2012). Mechanisms of CaMKII action in long-term potentiation. Nat. Rev. Neurosci. *13*, 169–182.

66. Herring, B.E., and Nicoll, R.A. (2016). Long-term potentiation: from CaMKII to AMPA receptor trafficking. Annu. Rev. Physiol. *78*, 351–365.

67. Hell, J.W. (2014). CaMKII: claiming center stage in postsynaptic function and organization. Neuron *81*, 249–265.

68. Diering, G.H., and Huganir, R.L. (2018). The AMPA receptor code of synaptic plasticity. Neuron *100*, 314–329.

69. Bayer, K.U., and Schulman, H. (2019). CaM kinase: still inspiring at 40. Neuron *103*, 380–394.

70. Hayashi, Y. (2022). Molecular mechanism of hippocampal long-term potentiation - towards multiscale understanding of learning and memory. Neurosci. Res. *175*, 3–15.

71. Wan, Y., Feng, G., and Calakos, N. (2011). Sapap3 deletion causes mGluR5-dependent silencing of AMPAR synapses. J. Neurosci. *31*, 16685–16691.

72. Jiang-Xie, L.F., Liao, H.M., Chen, C.H., Chen, Y.T., Ho, S.Y., Lu, D.H., Lee, L.J., Liou, H.H., Fu, W.M., and Gau, S.S. (2014). Autism-associated gene Dlgap2 mutant mice demonstrate exacerbated aggressive behaviors and orbitofrontal cortex deficits. Mol. Autism *5*, 32.

73. Welch, J.M., Lu, J., Rodriguiz, R.M., Trotta, N.C., Peca, J., Ding, J.D., Feliciano, C., Chen, M., Adams, J.P., Luo, J., et al. (2007). Cortico-striatal synaptic defects and OCD-like behaviours in Sapap3-mutant mice. Nature *448*, 894–900.

74. Welch, J.M., Wang, D., and Feng, G. (2004). Differential mRNA expression and protein localization of the SAP90/PSD-95-associated proteins (SAPAPs) in the nervous system of the mouse. J. Comp. Neurol. *472*, 24–39.

75. Ramírez-Armenta, K.I., Alatriste-León, H., Verma-Rodríguez, A.K., Llanos-Moreno, A., Ramírez-Jarquín, J.O., and Tecuapetla, F. (2022). Optogenetic inhibition of indirect pathway neurons in the dorsomedial striatum reduces excessive grooming in Sapap3-knockout mice. Neuropsychopharmacology *47*, 477–487.

76. Soto, J.S., Jami-Alahmadi, Y., Chacon, J., Moye, S.L., Diaz-Castro, B., Wohlschlegel, J.A., and Khakh, B.S. (2023). Astrocyte-neuron subproteomes and obsessive-compulsive disorder mechanisms. Nature *616*, 764–773.

77. Hadjas, L.C., Schartner, M.M., Cand, J., Creed, M.C., Pascoli, V., Lüscher, C., and Simmler, L.D. (2020). Projection-specific deficits in synaptic transmission in adult Sapap3-knockout mice. Neuropsychopharmacology *45*, 2020–2029.

78. Dani, A., Huang, B., Bergan, J., Dulac, C., and Zhuang, X. (2010). Superresolution imaging of chemical synapses in the brain. Neuron *68*, 843–856.

79. El-Husseini, A.E., Schnell, E., Dakoji, S., Sweeney, N., Zhou, Q., Prange, O., Gauthier-Campbell, C., Aguilera-Moreno, A., Nicoll, R.A., and Bredt, D.S. (2002). Synaptic strength regulated by palmitate cycling on PSD-95. Cell *108*, 849–863.

80. Wickner, W., and Schekman, R. (2008). Membrane fusion. Nat. Struct. Mol. Biol. *15*, 658–664.

81. Südhof, T.C., and Rothman, J.E. (2009). Membrane fusion: grappling with SNARE and SM proteins. Science *323*, 474–477.

82. Chen, X., Jia, B., Zhu, S., and Zhang, M. (2023). Phase separation-mediated actin bundling by the postsynaptic density condensates. eLife *12*, e84446.

83. Shen, N. (2023). 3D-STORM-data-process-with-MATLAB-app, version b2ca6a9, Software Heritage. https://github.com/NeoLShen/3D-STORM-data-process-with-MATLAB-app.git.

84. Bolte, S., and Cordelières, F.P. (2006). A guided tour into subcellular colocalization analysis in light microscopy. J. Microsc. *224*, 213–232.

85. Levet, F., Hosy, E., Kechkar, A., Butler, C., Beghin, A., Choquet, D., and Sibarita, J.B. (2015). SR-Tesseler: a method to segment and quantify localization-based super-resolution microscopy data. Nat. Methods *12*, 1065–1071.

86. Levet, F., Julien, G., Galland, R., Butler, C., Beghin, A., Chazeau, A., Hoess, P., Ries, J., Giannone, G., and Sibarita, J.B. (2019). A tessellation-based colocalization analysis approach for single-molecule localization microscopy. Nat. Commun. *10*, 2379.

Molecular Cell
Article

STAR★METHODS

KEY RESOURCES TABLE

REAGENT or RESOURCE	SOURCE	IDENTIFIER
Antibodies		
Mouse monoclonal anti-PSD95	Sigma	Cat#MAB1596
Rabbit polyclonal anti-Homer1	Synaptic Systems	Cat#160003
Rat monoclonal anti-Flag	Thermofisher	Cat#MA1-142-A488
Rabbit polyclonal anti-SAPAP3	Sigma	Cat#ABN325
Mouse monoclonal anti-beta actin	Proteintech	Cat#66009-1-Ig
Donkey anti-mouse IgG (H+L), CF®568	Biotium	Car#20802
Donkey anti-Rabbit IgG (H+L), Alexa Fluor® 647	Abcam	Cat#ab150075
IRDye® 800CW Goat anti-Mouse IgG Secondary Antibody	LI-COR	Cat#926-32210
IRDye® 800CW Goat anti-Rabbit IgG Secondary Antibody	LI-COR	Cat#926-32211
Chemicals, peptides, and recombinant proteins		
Recombinant protein: PSD-95 PSG(PDZ-SH3-GK)(aa 309R-724L, UniProt: P78352-1)	Zeng et al.[17]	N/A
Recombinant protein: PSD-95(aa 1M-724L, UniProt: P78352-1)	Zeng et al.[18]	N/A
Recombinant protein: SynGAP (CC-PBM)(aa 1147A-1308V, lacking 1192V-1193K and 1293E-1295G, UniPort: J3QQ18-1)		N/A
Recombinant protein: GKAP WT(3GBR-CT)(aa 328Q-421S+916Q-992L, UniProt: Q9D415-1)		N/A
Recombinant protein: Shank3 (NPDZ-HBS-CBS-SAM M1718E)(aa 533D-665R+ 1294D-1323P+ 1400A-1426P+1654G-1730S, M1718E, UniProt: Q4ACU6-1)		N/A
Recombinant protein: Homer1(aa 1M-366S, UniProt: Q9Z214-1)		N/A
Recombinant protein: Stg_CT, His$_6$-Stg_CT (aa 203D-323V; UniProt: Q3ZB20;His6-203D-323V; UniProt: Q3ZB20)	Zeng et al.[19]	N/A
Recombinant protein: PP2A (aa 1M-309L; Uniprot: P63330)	Cai et al.[60]	N/A
Recombinant protein: rCaMKIIα kinase domain (aa 1M-314S; UniProt: P11275)		N/A
Recombinant protein: Calmodulin(aa 1M-149K; UniProt: P0DP25)		N/A
Recombinant protein: GKAP SSA, SAS, ASS, SAA, ASA, AAS, AAA	This paper	N/A
Recombinant protein: GKAP* SSS, ASS, AAS		N/A
Recombinant protein: His$_8$-PSD-95 (His8-1M-724L, UniProt: P78352-1)		N/A
Recombinant : GKAP-1× DLS-SE, 1× DLS-SA, 3× DLS-SE or 3× DLS-SA		N/A
iFluor™ 488 succinimidyl ester	AAT Bioquest	Cat#1023
Cy3 monosuccinimidyl ester	AAT Bioquest	Cat#271
iFluor 555 maleimide	AAT Bioquest	Cat#1063
iFluor 488 maleimide	AAT Bioquest	Cat#1062
Alexa Fluor™ 647 succinimidyl ester	Invitrogen	Cat#A37566
Phos-Tag™ Acrylamide	Fujifilm	Cat#AAL-107

Continued

REAGENT or RESOURCE	SOURCE	IDENTIFIER
POPC	Avanti	Cat#850457P
PE-PEG5000		Cat#880230P
DGS-Ni-NTA		Cat#790404P
5-Fluro-2'-deoxyuridine	Sigma-Aldrich	Cat#F0503
Neurobasal Medium	Gibco	Cat#21103-049
B27	Gibco	Cat#17504044
GlutaMAX™ Supplement	Gibco	Cat#35050061
Penicillin-Streptomycin	**Gibco**	Cat#15070063
DNaseI	**Sigma-Aldrich**	Cat#DN25
Penicillin-Streptomycin	**Gibco**	Cat#15140122
Laminin Mouse Protein, Natural	**Gibco**	Cat#23017015
PDL	**Sigma**	Cat#P6407
Glucose Oxidase from Aspergillus niger	**Sigma**	Cat#G2133
Catalase from bovine liver	**Sigma**	Cat#C9322
Critical commercial assays		
Lipofectamine2000 transfection reagent	Invitrogen	Cat#11668019
Experimental models: Cell lines		
Escherichia coli BL21 (DE3) cells	Invitrogen	Cat# C600003
High Five inset cells	Thermo Fisher	Cat# B85502
Experimental models: Organisms/strains		
Mouse: embryonic day in vitro 16.5 hippocampal primary neuronal culture	N/A	N/A
AAV 2/9-hSyn-3×Flag	BrainVTA (Wuhan,China)	N/A
AAV 2/9-hSyn-3×Flag-SAPAP3 WT	BrainVTA (Wuhan,China)	N/A
AAV 2/9-hSyn-3×Flag-SAPAP3 S2A	BrainVTA (Wuhan,China)	N/A
AAV 2/9-hSyn-3×Flag-SAPAP3 2◇DLS-SE	BrainVTA (Wuhan,China)	N/A
AAV 2/9-hSyn-3×Flag-SAPAP3 2◇DLS-SA	BrainVTA (Wuhan,China)	N/A
Recombinant DNA		
Plasmid: 32M3C-PSD-95 PSG	Snead and Gladfelter[16]	N/A
Plasmid: 32M3C-Stg CT	Zeng et al.[18]	N/A
Plasmid: 32M3C-His₆-Stg CT		N/A
Plasmid: 32M3C-PSD-95	Zeng et al.[17]	N/A
Plasmid: 32M3C-GKAP		N/A
Plasmid: M3C-Shank3(NPDZ-HBS-CBS-SAM M1718E)		N/A
Plasmid: MG3C-SynGAP (CC-PBM)		N/A
Plasmid: M3C-Homer1		N/A
Plasmid: M3C-CaMKIIα (kinase domain, rat 1-314)	Cai et al.[60]	N/A
Plasmid:λ phosphatase		N/A
Plasmid: pFast-PP2A		N/A
Plasmid: MG3C-GKAP SSA, SAS, ASS, SAA, ASA, AAS, AAA	This paper	N/A
Plasmid: MG3C-GKAP* SSS, ASS, AAS		N/A
Plasmid: 32M3C-His₈-PSD-95		N/A
Plasmid: MG3C- GKAP-1× DLS-SE, 1× DLS-SA, 3× DLS-SE or 3× DLS-SA		N/A
Plasmid: pmCherry		N/A
Plasmid: GFP-SAPAP1		N/A
Plasmid: GFP-SAPAP1 3×DLS-SA, 3×DLS-SE		N/A
Plasmid: GFP-SAPAP3	Zhu et al.[51]	N/A

(Continued on next page)

Continued

REAGENT or RESOURCE	SOURCE	IDENTIFIER
Plasmid: GFP-SAPAP3 S2A		N/A
Software and algorithms		
Origin7.0	OriginLab	http://www.originlab.com/
PyMOL	PyMOL	http://pymol.sourceforge.net/
ImageJ	NIH	https://imagej.nih.gov/ij/
GraphPad Prism	GraphPad Software Inc	http://www.graphpad.com/scientific-software/prism/
ASTRA6	Wyatt	http://www.wyatt.com/products/software/astra.html
Matlab	MathWorks	https://ww2.mathworks.cn/products/matlab.html
Deposited data		
Imaging data	This paper	https://doi.org/10.17632/hj3897jwbw.1
Home-written codes	This paper; Shen[83]	https://doi.org/10.5281/zenodo.10065667

RESOURCE AVAILABILITY

Lead contact
Further information and requests for resources and reagents should be directed to and will be fulfilled by the lead contact, Mingjie Zhang (zhangmj@sustech.edu.cn).

Materials availability
Protein expression plasmids will be made available on request.

Data and code availability
All imaging data generated in this study have been deposited to Mendeley Data and are publicly available as of the date of publication under the https://doi.org/10.17632/hj3897jwbw.1.

The home-written codes and use of the codes for data analysis described in this manuscript have been deposited to Zenodo and are publicly available as of the date of publication. The DOIs are listed in the key resources table.

Any additional information required to reanalyze the data reported in this paper is available from the lead contact upon request.

EXPERIMENTAL MODEL AND STUDY PARTICIPANT DETAILS

Primary hippocampal neuron culture
Primary hippocampal neuron cultures were prepared from E16.5 C57BL/6 WT mice hippocampi (for transfection/ imaging). Digested cells were seeded on coverslips successively coated by poly-D-lysine (Sigma-Aldrich) and laminin (Gibco) in 12-well plates. Cells were plated for 4 hours in Neurobasal medium (Gibco) supported by 2 mM GlutaMax (Gibco), 2% (wt/vol) B27 supplement (Gibco), 50 U/ml penicillin, 50 mg/ml streptomycin and 10% FBS. Cells were maintained to DIV14 in neurobasal media supplemented with 2 mM GlutaMax, 2% (wt/vol) B27 (GIBCO). At DIV14, cells were transfected with 2 μg plasmids per well using Lipofectamine 2000 reagent (Invitrogen). Cells were fixed at DIV17 with 4% (wt/vol) paraformaldehyde (PFA) together with 4% (wt/vol) sucrose in 1× PBS (pH 7.5) and then mounted on slides for imaging.

Mice
WT and *Sapap3* KO mice (C57BL/6) were bred and raised under identical conditions in compliance with the guidelines set by the Institutional Animal Care and Use Committee at the animal core facility of the Huazhong University of Science and Technology in Wuhan, China. Mice were housed in groups of three to five per cage and maintained under a 12-hour light-dark cycle, with lights switched on at 8 a.m. The environment was kept at a consistent ambient temperature (21±1°C) and humidity (50±5%). Behavioral tests were conducted during the light phase of the cycle. *Sapap3*$^{-/-}$ mice were generated by Gem-Pharma-Tech Co Ltd, Nanjing, China (Primers: KO-F, 5'-TTGGTAGGCAATACCAACAGGG-3'; KO-R, 5'-TTGCGGTCCTTGCTCTTGCT-3'; WT-F, 5'-CCCTG AGCCTGAGTGAGGGT3'; WT-R, 5'-GGGAGTGTGTGGAAGCCATCT-3').

METHOD DETAILS

Protein expression and purification

Sequences coding various proteins were generated using standard PCR-based methods, each cloned into a vector containing an N-terminal Trx-His$_6$, or a GB1-His$_6$, or a His$_6$-affinity tag followed by an HRV 3C cutting site. All constructs were confirmed by DNA sequencing. Recombinant proteins were expressed in Escherichia coli BL21-CodonPlus (DE3)-RIL cells (Agilent) in LB medium at 16 °C overnight and protein expression was induced by 0.25 mM IPTG (final concentration) at OD$_{600}$ between 0.6-0.8.

Purifications of the cytoplasmic tail of Stargazin, PSD-95, a truncated form of SynGAP, a truncated form of GKAP, a truncated form of Shank3 and Homer1 were performed as described previously.[18,19] The boundary and sequence information of the proteins are detailed in the key resources table. Briefly, each recombinant protein was purified using a nickel-NTA agarose affinity column followed by a size-exclusion chromatography (Superdex 200 or Superdex 75, GE Healthcare) with a column buffer containing 50 mM Tris, pH 7.8, 100 mM NaCl, 2 mM DTT and 1mM EDTA. After cleavage by HRV 3C protease, the His$_6$, GB1-His$_6$ or Trx-His$_6$ tag was separated by another step of size-exclusion chromatography using Superdex 200 or Superdex 75 with the column buffer containing 50 mM Tris, pH 7.8, 100 mM NaCl, 2 mM DTT and 1mM EDTA.

For purifications of Homer1, a mono Q ion-exchange chromatography (GE Healthcare) was added to remove DNA contamination and His$_6$-tag after the HRV 3C protease cleavage. Protein was exchanged into a buffer containing 50 mM Tris, pH 7.8, 100 mM NaCl, 2 mM DTT and 1mM EDTA by a HiTrap desalting column (GE Healthcare).

Stg was expressed at 37 °C for 2 hours to minimize protein degradation. Proteins eluted from nickel-NTA agarose affinity column were then purified by Superdex 75 size-exclusion chromatography with a column buffer containing 50 mM Tris, pH 7.8, 300 mM NaCl, 2 mM DTT and 1mM EDTA. A mono S ion-exchange chromatography (GE Healthcare) was used to remove the Trx-His$_6$ tag from Stg after affinity tag cleavage by HRV 3C protease. Protein was exchanged into a buffer containing 50 mM Tris, pH 7.8, 100 mM NaCl, 2 mM DTT and 1mM EDTA by a HiTrap desalting column.

Purifications of calmodulin, CaMKIIα (kinase domain 1-314, rat) and PP2A followed the methods described in our previous work.[60] Kinases were co-expressed with λ phosphatase in Escherichia coli BL21-CodonPlus (DE3)-RIL cells. CaMKIIα kinase domain was purified using a nickel-NTA agarose affinity column followed by a size-exclusion chromatography (Superdex 75) with a column buffer containing 50 mM Tris, pH 7.8, 100 mM NaCl, 1mM EDTA, 2 mM DTT, and 10% glycerol. PP2A was expressed by Bac-to-Bac baculovirus expression system. The recombinant virus was generated by transposition, transfection, and serial steps of amplification using sf9 cells. For expression, cultured High Five cells (Thermo Fisher) with the density ~2.0 ×10^6 cells per mL were infected by baculovirus and incubated at 19°C for 120 h. Recombinant PP2A was firstly purified using Strep-Tactin XT Superflow resin (IBA) and then loaded onto a Superose 12 10/300 gel filtration column for final step purification with the buffer containing 50 mM Tris, pH 7.8, 100 mM NaCl, 2 mM DTT.

For His$_6$-Stg and His$_8$-PSD-95 used in SLB assays, the N-terminal His$_6$- or His$_8$ tag was placed right after the HRV 3C cutting site. The purification steps of His$_6$-Stg and His$_8$-PSD-95 are identical to ones for Stg and PSD-95.

The cDNA of Ser/Thr-free GKAP* sequences were commercially synthesized by BGI. PCR-amplified DNA fragments were cloned into the BamHI and XhoI sites on homemade mGB1-3C plasmid for protein expression. During cloning, Gibson assembly kit (NEB) was used to mutate the BamHI site from GGATCC to GGAGGC thus changing the protein coding from Gly-Ser to Gly-Gly. The purification method of GKAP* is identical to the purification of GKAP WT.

The purification of GKAP-1×DLS-SE, 1×DLS-SA, 3×DLS-SE or 3×DLS-SA is identical to the that of GKAP, despite a high-salt buffer containing 50 mM Tris, pH 7.8, 500 mM NaCl, 2 mM DTT and 1mM EDTA was used for 3× DLS-SE or 3× DLS-SA when running size exclusion column.

Protein fluorescence labeling

Amide labeling

Proteins were exchanged into a NaHCO$_3$ buffer (containing 100 mM NaHCO$_3$ pH 8.3, 300 mM NaCl, 1 mM EDTA and 2 mM DTT) and concentrated to 5-10 mg/mL. Alexa-647 NHS ester (Invitrogen) or iFluor-488/Cy3 NHS ester (AAT Bioquest) were dissolved in DMSO. Each dye and the protein to be labeled were mixed at a molar ratio of 1.5:1 and the reaction lasted for 1 hour at room temperature. Reaction was quenched by 200 mM Tris, pH 7.8. The unreacted fluorophores and other small molecules were removed from the proteins by passing the reaction mixture through a HiTrap desalting column with buffer containing 50 mM Tris, pH 7.8, 100 mM NaCl, and 2 mM DTT and 1mM EDTA.

Cysteine labeling

His$_6$-Stg were labeled at a specific site away from the His$_6$-tag and PBM in order to minimize any potential impact of the conjugated fluorophore on the protein's binding to SLBs and PSD-95.[19] Cys302, which is adjacent to PBM of Stg, was substituted with Ser. Ala212 was then converted to Cys for the single site fluorophore conjugation. The resulting His$_6$-Stg was prepared in a labeling buffer (50 mM Tris, pH 7.8, 300 mM NaCl, 1 mM EDTA and 1 mM TCEP) with final concentration of 2 mg/mL. iFluor-555 maleimide (AAT Bioquest) was added with 1.5:1 protein-to-fluorophore molar ratio and incubated for 1 h at room temperature. Unreacted fluorophore and other small molecules were removed from the protein by passing the reaction mixture through a HiTrap desalting column with buffer containing 50 mM Tris, pH 7.8, 300 mM NaCl and 1 mM TCEP.

For the labelling of His_8-PSD-95, five Cys restudies (Cys3, Cys5, Cys562, Cys626, Cys687) were mutated to Ser, Ser, Ala, Val and Ala, respectively. After mutagenesis, the only one Cys445 on the surface of SH3 domain was retained for site-specific Cys labeling as described above. ITC-based binding assay was used to verify that the mutations of five Cys residues on the GK domain did not affect the binding of PSD-95 to SAPAP (Data not shown). iFluor-488 maleimide (AAT Bioquest) was added with 1.5:1 protein-to-fluorophore molar ratio and incubated for 1 h at room temperature. The unreacted fluorophore and other small molecules were separated from the protein by a HiTrap desalting column with buffer containing 50 mM Tris, pH 7.8, 100 mM NaCl and 1 mM TCEP.

Fluorescence labeling efficiency was measured by Nanodrop 2000 (ThermoFisher). In imaging assays, fluorescence labeled proteins were further diluted with the corresponding unlabeled proteins in the same buffer. Dilution ratio was specified in the legend of each figure.

Imaging-based assay of phase separation

Imaging-based phase separation assays followed our previously described procedures.[18] Briefly, proteins (with affinity tags cleaved and removed) were prepared in a buffer containing 50 mM Tris, pH 7.8, 100 mM NaCl, 2 mM DTT, 1mM EDTA and pre-cleared via high-speed centrifugations. Proteins were then mixed or diluted with buffer to designated combinations and concentrations. For phase separation assay involving $CaMKII\alpha$, PSD proteins were mixed in a buffer containing 50 mM Tris, pH 7.8, 100 mM NaCl, 2 mM DTT, 0.5mM ATP, 1mM $CaCl_2$ and 1mM $MgCl_2$. After 10 mins incubation, the protein mixture was injected into a homemade flow chamber for DIC and fluorescent imaging with a Nikon Ni-U upright fluorescence microscope (20× and 40× lenses) or with a Zeiss LSM880 confocal microscope (20×, 40× and 63× lenses). Images were analyzed by the ImageJ software.

For sedimentation assays, 50 μL of protein mixture was equilibrated at room temperature for 10 mins before it was subjected to sedimentation at 16,873 g for 10 min at 23°C on a table-top temperature-controlled micro-centrifuge. After centrifugation, the supernatant and pellet were immediately separated into two tubes. The pellet fraction was dissolved with 50 μL buffer plus 50 μL 2× SDS loading dye. Proteins from both supernatant and pellet were analyzed by SDS-PAGE with Coomassie blue staining. Band intensities were quantified using the ImageJ software.

CaMKIIα auto-phosphorylation

$CaMKII\alpha$ kinase domain (100 μM) was first mixed with 200 μM calmodulin for auto-phosphorylation in a buffer containing 50 mM Tris pH 7.8, 100 mM NaCl, 10 mM ATP, 5 mM $CaCl_2$, 2 mM DTT, 5 mM $MgCl_2$ and 10% glycerol at room temperature for 10 min. Active $CaMKII\alpha$ were used for both phase separation assay and GKAP *in vitro* phosphorylation assay.

GKAP/GKAP* *in vitro* phosphorylation

Each variant of GKAP/GKAP* protein at 20 μM was mixed with 0.5 μM auto-phosphorylated $CaMKII\alpha$ kinase domain in a reaction buffer containing 50 mM Tris pH 7.5, 100 mM NaCl, 10 mM ATP, 2 mM DTT and 5 mM $MgCl_2$ at room temperature overnight. To remove the enzymes after phosphorylation, samples were passed through a Superdex 75 size-exclusion column with buffer containing 50 mM Tris, pH 7.8, 100 mM NaCl, 2 mM DTT and 1mM EDTA.

Phos-Tag™ SDS-PAGE

Proteins mixed with 2X SDS loading buffer were loaded into homemade Phos-Tag SDS-PAGE gel composed of a 4% (w/v%) polyacrylamide stacking gel and 12.5% (w/v%) polyacrylamide resolving gel. During the preparation of resolving gel, 25 μM Phos-Tag™ Acrylamide (Fujifilm) and 125 μM $MnCl_2$ were added for separating phosphorylated proteins.

Lipid bilayer preparation and phase separation assay

Lipid bilayer phase separation assay followed our previously described procedures.[18,19] Supported membrane bilayers were made of 97.9% POPC, 2% DGS-NTA-Ni^{2+} and 0.1% PE-PEG5000. 2 μM His_8-PSD-95 was added and incubated with SLBs for 1 h at room temperature, followed by washing with the cluster buffer (50 mM Tris, pH 7.8, 100 mM NaCl, 1 mM TCEP, 1 mg/mL BSA) for three times to remove unbound protein. The His_8-PSD-95-coated SLBs was next incubated with 50 nM His_6-Stg for 5 mins. After His_6-Stg coating, PSD proteins were added to the SLB-containing chamber to induce phase separation on the lipid bilayers. Protein clusters formed on SLBs were imaged with a Zeiss LSM880 confocal microscope (63×lens). Imaging data was analyzed by the ImageJ software. 5% fluorescence labelling was used for both His_8-PSD-95 and His_6-Stg to obtain high-quality imaging data. The PP2A-mediated cluster dispersion was recorded with a Nikon Eclipse Ti2 microscope with a 63×lens operated in the TIRF mode.

Isothermal titration calorimetry assay

ITC measurements were carried out on a MicroCal VP-ITC calorimeter at 25 °C. Proteins used for ITC measurements were dissolved in an assay buffer composed of 50 mM Tris, pH 7.8, 100 mM NaCl, 2 mM DTT and 1 mM EDTA. Affinity tags on proteins were cleaved and removed. High concentration of protein was loaded into the syringe and titrated into the cell containing low concentration of corresponding interactors (concentrations for each reaction are indicated in the figure legends). For each titration point, a 10 μL aliquot of a protein sample in the syringe was injected into the interacting protein in the cell at a time interval of 2 min. Titration data were analyzed using the Origin7.0 software and fitted with the one-site binding model.

Fast protein liquid chromatography coupled with static light scattering

The analysis was performed on an Agilent InfinityLab system coupled with a static light scattering detector (miniDawn, Wyatt) and a differential refractive index detector (Optilab, Wyatt). Protein samples with indicated concentrations were loaded to a Superose 12 10/300 GL column (GE Healthcare) pre-equilibrated with 50 mM Tris, pH 7.8, 100 mM NaCl, 2 mM DTT and 1 mM EDTA buffer. Data were analyzed using ASTRA 6 software (Wyatt).

Single molecule tracking for 3D phase separation system

STORM based single molecule tracking was performed to measure the dynamics of the proteins in 3D phase separation system. For each single molecule tracking experiment, only one protein (PSD-95/Shank3) was very sparsely labelled with Cy3 (at 0.01%). Before tracking, each sample was mixed with a freshly prepared imaging buffer (0.5% D-glucose(wt/vol), 0.56 μg/mL glucose oxidase (Sigma), 4 μg/mL catalase (Sigma) and 10 mM beta-mercaptoethanol). Imaging of each sample was completed within half hour upon the addition of the imaging buffer.

A Zeiss Elyra7 microscope with a 63x (N.A.=1.4) oil objective lens was used to capture and analyze captured images. A wide field image was captured first with 2% of the full power (500 mW) of a 561nm laser. Prior to dSTORM imaging, the 3D phase separation sample was bleached with 50% of the full power of 561nm laser for 30 seconds with EPI mode. dSTORM images were acquired under 50% of the full power of 561nm laser with the HILO mode and a TIRF-hp filter was used during imaging. All images were captured with 3,000 frames with an exposure time of 30ms per frame. Auto focus with the "definite focus" strategy was performed at every 500 frames. The raw data was then processed by home-written MATLAB programs to get molecule tracks.[57] All tracks that localized that in the PSD-95/Shank3 enriched region and track length longer than 10 frames were selected to calculate the mean squared displacement (MSD) curve with their first 10 displacements. The apparent diffusion coefficient was calculated by fitting the MSD curve with the function of MSD=4Dt+C.

Behavioral analysis

For grooming behavior analysis, each mouse (2-5 months old, male) was video-recorded alone in the PhenoTyper home cage (40× 40×40 cm, Noldus, Holland), which provided a home environment for mice, with sufficient food and water supply. Animal behaviors were detected by the interruption of an infrared beam by the animal body, monitored between 10 a.m.-1 p.m. or 1 p.m.-4 p.m. We used EthoVisionXT (Noldus, Holland) for automated video analysis to measure the grooming time over a span of three hours.

Stereotaxic injection

Sapap3⁻/⁻ mice (C57BL/6, 5-6 weeks old, either male or female) were anesthetized with chloral hydrate and secured in a stereotaxic device to immobilize the head and expose the skull. Burr holes were drilled at planned injection sites. At each site, the microinjection needle was first advanced to the deepest (ventral) position of striatum for an initial injection; subsequent injections were made every 0.4mm or 0.5mm while retracting the injection needle. Bregma coordinates were as follows: for injection site 1, location 1-4: anteroposterior 0.3mm, mediolateral 2.2mm, dorsoventral 4.0, 3.6, 3.2, 2.8mm; for injection site 2, location 5-7: anteroposterior 1.0mm, mediolateral 1.3mm, dorsoventral 3.75, 3.25, 2.75mm. At each injection location, 300nl of the AAV virus (3×10¹²vg/ml; vector genome/ml) was administered using a microsyringe (World Precision Instruments), with the needle left in place for 6 minutes at the medium location and 8 minutes at the top and bottom locations.

Immunohistochemistry

One month after virus injection, *Sapap3*⁻/⁻ mice were sacrificed by intraperitoneally injection of an overdose of chloral hydrate and were transcardially perfused with 20ml PBS (pH=7.4). Brains were dissected out and freshly frozen by embedding into tissue-tek OCT medium and placing the tissue blocks into dye ice pre-cooled isopentane. Sections of 5μm thickness were cut on a cryostat (Minux® Cryostats, RWD) and collected on glass coverslips. Sections were fixed for 10 min with 4% PFA (wt/vol) in PBS, followed by washing off excess PFA and quenching with 20mM glycine in PBS. Sections were then blocked and permeabilized using 3% BSA (wt/vol) in PBS with 0.1% Triton X-100 (vol/vol), following by incubation with primary antibody (1:500 mouse anti-PSD95, Sigma; 1:3000 rabbit anti-Homer, Synaptic Systems and 1:500 Alexa 488-rat anti-Flag, Thermofish) in blocking buffer overnight at 4°C and wash 6 times in PBS. Then, the sections were incubated with secondary antibodies (1:500 CF568 donkey anti-mouse, Biotium; 1:5000 Alexa 647 donkey anti-rabbit, Abcam) in blocking buffer 2h at room temperature, and then wash 6 times in PBS. Finally, the sections were fixed for 5 min in 3% PFA (wt/vol) after antibody labeling.[78]

Western blot

Brain tissues were isolated from Sapap3⁺/⁺ and Sapap3⁻/⁻ mice (4 months old, male) and homogenized on ice using a High-Throughput Tissue Homogenizer in 1 ml of HEPES-buffered sucrose (0.32 M sucrose, 10mM HEPES, 1 mM EDTA, pH 7.4), supplemented with protease inhibitors. The resulting lysate was then centrifuged at 1000×g at 4°C to separate the pelleted nuclear fraction (P1). The supernatant (S1) was further centrifuged at 12000×g for 20 minutes to yield pellet P2 (which contains synaptosome). This pellet was resuspended in 100 μL of ice-cold HEPES buffer (4 mM HEPES, 1 mM EDTA, pH 7.4) and mixed for 20 minutes at 4°C. The lysate was again centrifuged at 12,000×g for 20 minutes to obtain the pellet P3. The P3 fraction was resuspended in 100 μl of ice-cold buffer A (20 mM HEPES, 100 mM NaCl, 0.5% Triton X-100 (vol/vol), pH 7.4), gently agitated for 15 minutes at 4°C, and then

centrifuged at 12, 000×g for 20 minutes. The resultant pellet was resuspended in 120 μl of ice-cold buffer (20 mM HEPES, 150 mM NaCl, 1% Triton X-100, 1% deoxycholic acid, 1% SDS, 1 mM DTT, pH7.4), gently agitated for 1 hour at 4°C, and centrifuged at 12000×g for 20 minutes. The collected supernatant represents the PSD fraction. The PSD fractions were combined with beta-mercaptoethanol (final concentration 5%, (vol/vol)) and bromophenol blue (final concentration 0.05%, (wt/vol)), then boiled for 10 minutes. The boiled mixtures were loaded onto SDS-PAGE and subsequently transferred to nitrocellulose membranes (GE Healthcare Bio-Science). The membranes were blocked with 5% non-fat milk (wt/vol) in 1x PBS for 1 hour at room temperature, followed by incubation with primary antibodies (1:1000 rabbit anti-mouse, Sigma; 1:20000 mouse anti-beta actin, Proteintech). After three washes with TBST buffer, the membranes were incubated with appropriate secondary antibodies (1:10000 IRDye®800CW anti-mouse/rabbit, LI-COR Biosciences) for 1 hour at room temperature. The membranes were then scanned using the Odyssey® CLX Infrared Imaging System (Odyssey, LI-COR).

dSTORM image acquisition

Before dSTORM imaging, each brain slice was exchanged into a freshly prepared imaging buffer (5% D-glucose (wt/vol), 5.6 μg/mL glucose oxidase (Sigma), 40 μg/mL catalase (Sigma) and 150 mM beta-mercaptoethanol) and transferred into a homemade chamber. Imaging of each sample was completed within an hour upon the addition of the imaging buffer.

A Zeiss Elyra7 microscope with a 63× (N.A.=1.4) oil objective lens was used to capture and analyze the dual channel images for each brain slice sample. A wide field image was captured first with 2% of the full power (500mW) of 488nm/561nm/647nm laser. Prior to dSTORM imaging, the brain slice sample was bleached with 100% of the full power of 561nm/647nm laser at least 3 minutes with EPI mode to reduce background signal level. Auto focus with the "definite focus" strategy was performed at every 300 frames during bleaching. dSTORM images were acquired under 100% of the full power of 561nm/647nm laser with the HILO mode and a TIRF-ultrahp filter were used during imaging. All images were captured with 15,000 frames with an exposure time of 30ms per frame. Auto focus with the "definite focus" strategy was performed at every 300 frames during image acquisitions. Alignment of dual channels was performed before imaging.

QUANTIFICATION AND STATISTICAL ANALYSIS

Quantification of colocalization

The localization analysis was performed by analyzing the Pearson's correlation coefficient of 488-PSD-95 and 647-Shank3 fluorescence foci using the Image J Fiji plugin JACoP.[84]

Quantification of cluster area in SLBs

The Image J Fiji was used to quantify the cluster area in supported lipid bilayer. The intensity of the background signal (I_{min}) and the intensity of the highest signal inside clusters (I_{max}) was measured first. Any cluster with size larger than $0.1 \mu m^2$ and with mean signal intensity above (I_{max}+ I_{min})/2 were passed by filter. The areas of the clusters were measured by the plugin application of the Image J software. The imaging acquisition and analysis settings were kept the for the images acquired in different group.

Quantification of dSTORM imaging for brain slice

Synapses were first manually identified in the wide field image. The corresponding PSD clusters of super resolution localizations in synapses were then selected manually with the help of the tessellation-based auto clustering algorithm.[85,86] The selected PSD clusters were then used to calculate the distance between PSD-95 localization plane and Homer1 localization plane by a homemade MATLAB program with the same strategy as described before.[78] PSD clusters that are with less than 100 localizations were excluded from the quantifications.

Statistical parameters including the definitions and exact values of n (e.g., number of experiments, number of spines, number of cells, etc.), distributions and deviations are reported in the figures and corresponding figure legends. Data of in vitro phase separation imaging assay are expressed as mean ± SD. Data of primary mice neuron culture are expressed as mean ± SD; ns, not significant, *p < 0.05, **p < 0.01, ***p < 0.001 and ****p < 0.0001 using student T-test or one-way ANOVA with Tukey's multiple comparison test.

Data are judged to be statistically significant when p < 0.05 by one-way ANOVA with Tukey's multiple comparison test. None of the data were removed from our statistical analysis as outliers. Statistical analysis was performed in GraphPad Prism. All experiments related to cell cultures and imaging studies were performed in blinded fashion.